The spatial structure of feedforward information in mouse primary visual cortex

Jun Zhuang, Rylan S. Larsen, Kevin T. Takasaki, Naveen D. Ouellette, Tanya L. Daigle, Bosiljka Tasic, Jack Waters, Hongkui Zeng, R. Clay Reid

Abstract

The projection from lateral geniculate nucleus (LGN) to primary visual cortex (V1) is organized into parallel pathways in carnivores and primates. But such a model has not been thoroughly tested in mice, a popular model species for visual physiology. By measuring the calcium activity of LGN axons in V1 of awake mice, we show that the motion-sensitive axons and location-sensitive axons are largely separate. The motion-sensitive axons prefer low temporal frequencies (TFs) and high spatial frequencies (SFs) and show a depth-dependent direction bias, while the location-sensitive axons respond to wide SF and TF spectrum and show a depth-independent OFF dominance. Furthermore, the motion-sensitive axons have greater horizontal bouton spread than the location-sensitive axons but, within each group, the bouton spread is largely uniform. In summary, our results demonstrate that there are at least two parallel thalamocortical pathways in mouse visual system with distinct functional properties, spatial distributions, and axonal morphologies.

Introduction

Parallel pathways along hierarchical processing stages are a prominent feature of early visual systems in carnivores (Stone et al., 1979; Lennie, 1980) and primates (Nassi and Callaway, 2009), where structured thalamocortical projections from dorsal lateral geniculate nucleus (LGN) to primary visual cortex (V1) serve as major inputs to cortical computations and shape the cortical single-cell response properties (i.e. orientation selectivity, Hubel and Wiesel, 1962; Reid and Alonso, 1995) as well as the functional architecture at larger scale (orientation map and ocular dominance map, Jin et al., 2011; Kremkow et al., 2016).

In the last decade, the mouse visual system has become a popular model system to study visual physiology due to its experimental tractability and the availability of genetic tools. When compared with higher mammals, the mouse LGN shows more diverse response properties. Particularly, besides cells with canonical ON and/or OFF concentric receptive fields (Grubb & Thompson, 2003), a significant portion of the cells in mouse LGN are sensitive to motion (Marshel et al., 2012; Piscopo et al, 2013; Zhao et al., 2013; Scholl et al., 2013; Durand et al., 2016) which may be inherited from its retinal inputs (Huberman et al, 2009; Cruz-Martin et al, 2014; Rompani et al., 2017; Dhande et al., 2015). How this motion information is transmitted at the thalamocortical stage is less clear. It has been proposed that the motion information is conveyed by the direction-selective (DS) cells from LGN shell to the superficial layer of V1 while the location information is conveyed by cells in LGN core with concentric receptive fields to deeper layers (Cruz-Martin et al., 2014, Seabrook et al., 2017), similar to the parallel pathways in carnivores and primates. But the evidence for this layer-specific distribution is scarce and

43 controversial: while one study found mouse layer 4 in V1 receive slightly less DS LGN inputs
44 than layer 1 (Kondo et al., 2016), another study showed layer 4 receives the same amount of DS
45 inputs as superficial layers (Sun et al., 2016). On the other hand, how LGN inputs are distributed
46 along with the V1 retinotopic organization has not been investigated. Given the unique
47 functional architecture of rodent V1 (Okhi et al., 2007), it may or may not be the same as what
48 has been found in other species (Jin et al, 2008; Yeh et al., 2009; Kremkow et al., 2016; Lee et
49 al., 2016).

50 To investigate the spatial distributions of LGN inputs in V1, we used genetic and viral tools to
51 label mouse LGN neurons with calcium indicators and systematically measured the response
52 properties of their axon terminals in V1 at different depths. We found the inputs sensitive to
53 motion and inputs sensitive to location are largely separate, forming two parallel pathways.
54 Comparing to the location pathway, the axons in the motion pathway prefer stimuli with low
55 temporal and high spatial frequencies and have greater bouton spread in horizontal dimension.
56 Furthermore, the motion pathway shows a depth-dependent bias in preferred direction while
57 the location pathway shows a depth-independent OFF dominance. Our findings demonstrate
58 there are at least two parallel thalamocortical pathways with distinct functional and structural
59 properties in mouse visual system.

60

61 # Results

62 **Selective labeling and functional imaging of feedforward visual inputs from LGN to V1.**

63 To image LGN axons in V1, we used the Vipr2-IRES2-Cre-neo transgenic mice. Crossing Vipr2-
64 IRES2-Cre-neo mice with reporter line Ai14 drove tdTomato expression in the cells from LGN,
65 ventral posterolateral nucleus, ventral posteromedial nucleus of thalamus, suprachiasmatic
66 nucleus and central amygdala nucleus but not in the lateral posterior nucleus of thalamus and
67 cortex (Fig. 1a left, Allen Brain Atlas Transgenic Characterization Experiments: 576523754,
68 576524006, 577720920, 577721229). In V1, densely labeled axons were visible in layer 1
69 through layer 4 (Fig. 1a right). Among the tdTomato positive nuclei, only LGN projects to V1,
70 suggesting that the labeled axons in V1 are from LGN and carry feedforward visual information.
71 To express calcium indicator in thalamocortical LGN axons, we injected a mixture of AAV viruses
72 containing Cre-dependent GCaMP6s and Cre-independent mRuby directly into the LGN of
73 Vipr2-IRES2-Cre-neo mice (Fig. 1b). Three weeks after injection, the somatic expression of
74 GCaMP was restricted in LGN while mRuby was expressed along the injection track through
75 cortex and hippocampus (Fig. 1c left). There was extensive GCaMP labeling of thalamocortical
76 axons throughout superficial and middle layers in V1, indicating the calcium indicator has been
77 transported to the axons (Fig. 1c right).

78 We performed two-photon calcium imaging of LGN axons 50-400 µm below the pia in awake
79 mouse V1 (Fig. 1d). The imaging was done in a columnar fashion: for a given cortical location,
80 calcium signals from boutons were collected from 3 to 8 planes at different depths under pia. In
81 total, 26 volumes (158 image planes from 6 mice) were imaged and calcium activity traces were

82 extracted from 50171 regions of interest (ROIs) representing putative boutons (Supplementary
83 Table 1). During each imaging session, we measured spatial receptive fields (RFs) with a locally
84 sparse noise stimulus (Methods), tuning for orientation/direction, spatial/temporal frequency
85 (SF, TF) with drifting gratings, and spontaneous activity. Many ROIs showed strong calcium
86 activities (Fig. 1e,f., Supplementary video 1), significant spatial RFs (Fig. 1g, j) and responses to
87 gratings (Fig. 1h,i). In some experiments, aberrations were reduced with adaptive optics,
88 thereby increasing fluorescence intensity and signal-to-noise ratio (Supplementary Fig. 2). The
89 data from imaging sessions with and without adaptive optics were substantially similar, so
90 sessions from both conditions were pooled together. In summary, our labeling strategy enabled
91 us to selectively label LGN neurons and characterize the functional properties of their axons in
92 V1.

93

94 **LGN boutons can be grouped into axons based on highly correlated activities.**

95 To map individual sources of LGN inputs to V1, it is necessary to distinguish boutons that are
96 from the same axon from pairs that are from different axons. The boutons from an individual
97 axon should have a higher level of correlation in their activity than the boutons from different
98 axons. In our data, there were subgroups of putative boutons showing highly correlated activity
99 in each imaging plane indicating that they were likely from same axons (Fig. 2b). To identify
100 these subgroups, we calculated an event-based pair-wise correlation between all pairs of
101 boutons in each imaging plane, followed by hierarchical clustering (Fig. 2, Methods, modified
102 from Liang et al., 2018). Overall, the clustering faithfully preserved the pairwise correlation

103 distance (Fig. 2e, mean cophenetic correlation distance = 0.89 ± 0.03, range = 0.80 - 1.00,
104 n=158) and the correlation coefficients from bouton pairs within and between clusters showed
105 non-overlapping distribution (Fig. 2g). The boutons from a single cluster show highly correlated
106 calcium activity (Fig. 2b) and response properties (Fig. 2c, 2d), further confirming their high
107 likelihood of being from single axons. For the imaging sessions with spontaneous activity
108 recordings, we found the clusters generated with entire calcium traces also represented the
109 correlation structure of spontaneous activities (Fig. 2f), thus all imaging planes were processed
110 using the whole calcium activity traces for bouton clustering. We use "bouton" to refer
111 individual ROI, "axon" to refer to a group of boutons with high temporal correlations, and
112 "unit" to refer to either entity. For each axon, we used average calcium traces from all of its
113 boutons to calculate its own response properties. Overall, the axon to bouton ratio (per plane)
114 is consistent across cortical depth (Fig. 2h, one way ANOVA across depth: F=1.19, p=0.31. mean
115 of all depths: 0.53 ± 0.01).

116

117 **Two populations of LGN axons with distinct functional and structural properties.**

118 We found no depth-dependent differences in population average of measured response
119 properties except preferred spatial frequency which increases along with cortical depth
120 (Supplementary Fig. 1, global direction selectivity index, gDSI, boutons: 0.40 ± 0.003, F=0.34,
121 p=0.93; axons: 0.38 ± 0.003, F=0.31, p=0.95; global orientation selectivity index, gOSI, boutons:
122 0.28 ± 0.003, F=0.55, p=0.80; axons: 0.27 ± 0.003, F=0.77, p=0.61; preferred temporal
123 frequency, boutons: 2.70 ± 0.10 Hz, F=1.07, p=0.39; axons: 2.83 ± 0.09 cpd, F=0.53, p=0.81; RF

strength, boutons: 1.89 ± 0.02, F=0.77, p=0.61; axons: 1.87 ± 0.02, F=0.61, p=0.74; preferred spatial frequency, boutons: 0.090 ± 0.004 cpd, F=5.87, $p=9x10^{-6}$; axons: 0.085 ± 0.003 cpd, F=4.17, $p=4x10^{-4}$. One-way ANOVA). These results are consistent with the previous report (Sun et al, 2016) but do not support the prediction of depth-dependent projection of motion-sensitive inputs (Cruz-Martin et al., 2014; Seabrook et al., 2017). We then focused our analysis on the two functional properties: spatial receptive field and direction selectivity, which are most likely to represent parallel pathways suggested by previous studies (Piscopo et al., 2013; Cruz-Martin et al., 2014; Seabrook et al., 2017). We found the units with significant spatial receptive fields (Methods) were more likely to have low direction sensitivity (gDSI) than the axons without significant spatial RFs (nRF, Fig. 3a) while the DS units were more likely to have low RF strength than non-DS (nDS) units (Fig. 3b) and only a small portion of units had both significant spatial RF and direction selectivity (RFDS boutons 5.32% of all boutons, RFDS axons: 5.15% of all axons, Fig. 3c,d) in the entire population.

Do these two functionally separated groups differ in other aspects? To answer this question, we first compared the preferred SF and TF between DS and RF groups. We found while the distribution of preferred TF and SF from the RF units spread widely across the spectrum tested, the distributions from the DS units were concentrated to high SFs and low TFs (Fig. 1e, 1f respectively, SF: DS boutons vs. RF boutons, 0.102 ± 0.036 vs. 0.004 ± 0.063 cpd, U=188907, $p<10^{-100}$; DS axons vs RF axons, 0.098 ± 0.035 vs. 0.043 ± 0.061 cpd, U=53118, $p<10^{-100}$; TF: DS boutons vs. RF boutons, 1.45 ± 0.59 vs. 2.56 ± 2.80 Hz, U=9421173, $p<10^{-100}$; DS axons vs. RF axons: 1.46 ± 0.59 vs. 2.51 ± 2.70 Hz, U=1917535, $p<10^{-100}$). This observation is consistent with extracellular electrical recordings from LGN neurons in both anesthetized (Piscopo et al., 2013)

146 and awake animals (Allen Visual Coding With Neuropixels dataset, https://portal.brain-
147 map.org/explore/circuits/visual-coding-neuropixels, Siegle et al., 2019), which shows a negative
148 correlation between direction selectivity and preferred TF (linear regression, slop=-9.284,
149 p=0.00086, Supplementary Jupyter Notebook). Secondly, we compared the axon masks in our
150 imaging planes between DS and RF axons. We first aligned the binary mask of each axon to its
151 own center of mass and picked those with at least two boutons. We summed all the aligned
152 axon masks for all DS and all RF axons. Since DS and RF axons have different counts, we divided
153 the summed DS and RF axon masks to their own peaks, generating a normalized population
154 axon mask for each group. The results show a drastic difference in the axon structure between
155 DS and RF populations with DS axons having substantially greater bouton spread than RF axons
156 (Fig. 3g). To quantify this difference, we compared multiple metrics measured from the axon
157 masks between DS and RF groups. Consistently, the DS axons showed significantly higher
158 bouton counts (Fig. 3h, DS axons: 2.94 ± 0.01; RF axons: 2.54 ± 0.06; nRFnDS axons: 3.30 ± 0.08.
159 DS vs RF: t=563, $p=7.0\times10^{-5}$, DS vs nRFnDS: t=612, $p=2.2\times10^{-4}$, RF vs nRFnDS: t=93, $p=1.7\times10^{-11}$,
160 Wilcoxon rank test), max bouton distances (Fig. 3i, DS axons: 94.5 ± 2.1 µm; RF axons: 88.3 ± 1.8
161 µm; nRFnDS axons: 95.6 ± 2.0 µm. DS vs RF: t=263, p=0.03, DS vs nRFnDS: t=411, p=0.80, RF vs
162 nRFnDS: t=255, p=0.008, Wilcoxon rank test) and larger axon coverage area (Fig. 3j, DS axons:
163 2362 ± 122 μm^2; RF axons: 2162 ± 107 μm^2; nRFnDS axons: 2480 ± 126 μm^2. DS vs RF: t=236,
164 p=0.01, DS vs nRFnDS: t=404, p=0.73, RF vs nRFnDS: t=192, p=0.002, Wilcoxon rank test) than
165 RF axons, indicating that the DS axons have more extensive axon arbors than RF axons. In
166 summary, our data showed there are at least two subpopulations of LGN inputs forming
167 parallel channels, with one carrying motion information (DS units) and the other carrying

168 location information (RF units). Furthermore, the DS axons prefer higher SF and lower TF and
169 have larger axon arbors than the RF axons. Strikingly, we found no depth dependence in the
170 number of DS and RF units up to 400 µm from the pia surface (Supplementary Fig. 3).

171

172 **Depth-dependent motion direction bias in the motion channel**

173 We next examined the preferred direction distribution in the motion channel, which strongly
174 biased towards nasal and temporal directions (Fig. 1l) consistent with a previous report
175 (Marshel et al., 2012). Interestingly, in a given image plane the DS population was often biased
176 towards either nasal or temporal direction (i.e. bias toward the temporal direction in the
177 example plane, Fig. 1k). When broken into different depths, the preferred direction distribution
178 of DS boutons showed a marked trend across cortical depth: the preferred direction bias
179 gradually switched from strongly nasal at 50 µm to strongly temporal at 400 µm (Fig. 4a). To
180 quantify the differences in preferred direction bias, for a given population of DS units that
181 preferred nasal or temporal directions, we defined a metric called nasal-temporal index (NTI),

182 $$NTI = (n_{nasal} - n_{temporal}) / (n_{nasal} + n_{temporal}) ,$$

183 in which n_{nasal} and $n_{temporal}$ represents the number of boutons preferring each direction.
184 Consistent with the observations above, the superficial (< 225 µm) boutons had a nasal bias
185 (NTI = 0.245, Fig. 4b magenta), and the deep (> 225 µm) boutons had a temporal bias (NTI =
186 0.259, Fig. 4b, green). This trend was significant across all mice (Fig. 4c, n=6, superficial vs.
187 deep, 0.22 ± 0.09 vs. -0.11 ± 0.11, Wilcoxon rank test, T=0, p=0.028) and all volumes (Fig. 4d,

188 n=17, superficial vs. deep, 0.25 ± 0.10 vs. -0.03 ± 0.12, Wilcoxon rank test, T=17, p=0.005).
189 Similarly, the preferred directions of axons showed a same trend (Fig. 3e-h, NTI superficial vs.
190 deep, for mice: n=6, 0.26 ± 0.06 vs. -0.14 ± 0.12, T=0, p=0.028; for volume: n=14, 0.34 ± 0.10 vs.
191 -0.01 ± 0.11, t=6, p=0.0035, Wilcoxon rank test). Furthermore, this trend held true when
192 considering direction selectivity strength of individual units (Supplementary Fig. 4) and was
193 insensitive to the threshold of direction selectivity (Supplementary Fig. 5). In summary, the
194 motion channel of LGN input to V1 showed nasal to temporal direction bias change along with
195 cortical depth.

196

197 **OFF dominance in the location channel.**

198 Similar to previous reports from other species (Jin et al., 2008; Yeh et al., 2009), our RF units
199 showed a strong OFF dominance in LGN inputs to V1. There were significantly more OFF
200 subfields than ON subfields measured from all boutons (Fig. 5a, all depths, subfields per plane:
201 n=121, ON vs. OFF, 54.5 ± 31.7 vs. 73.3 ± 52.1, Wilcoxon rank test, T=1471, $p=4.3x10^{-8}$) and this
202 difference was consistent across cortical depth (ON vs. OFF, superficial: n=73, 53.6 ± 31.5 vs.
203 72.8 ± 52.7, T=536, $p=1.3x10^{-5}$; deep: n=48, 55.8 ± 31.9 vs. 74.2 ± 51.1, T=234, $p=8.1x10^{-5}$,
204 Wilcoxon rank test). Additionally, the OFF subfields were significantly larger than ON subfields
205 (Fig. 5b, all depths, ON vs. OFF: n=121, 83.3 ± 2.0 vs. 102.1 ± 2.7 deg^2, T=1480, $p=1.1x10^{-8}$,
206 Wilcoxon rank test) also consistently across depth (ON vs. OFF, superficial: n=73, 81.5 ± 2.4 vs.
207 102.1 ± 3.8 deg^2, T=532, $p=6.8x10^{-6}$; deep: n=48, 86.0 ± 3.4 vs. 102.0 ± 3.5 deg^2, T=240,
208 $p=3.6x10^{-4}$, Wilcoxon rank test). Since we used an adaptive threshold to extract RF (Methods),

209 having larger OFF RF areas is equivalent to having stronger OFF responses. Similar OFF
210 dominance was also observed in axons (Fig. 5c,d, ON vs. OFF, n=116, subfields per plane: 25.3 ±
211 1.4 vs. 33.8 ± 2.2, T=1436.5, p=1.2x10-7; subfield area: 85.5 ± 1.8 vs. 100.9 ± 2.4 deg2, T=1358,
212 p=2.1x10-8; Wilcoxon rank test).

213 Another form of "OFF dominance", reduced retinotopic scatter for OFF cells, that was
214 prominent in other mammalian species (Kremkow et al., 2016; Lee et al., 2016), also presented
215 in our data. For a given plane, we calculated the normalized retinotopic location of all ON and
216 OFF subfields as the form of z-scores by subtracting the population RF center and dividing the
217 standard deviation (Methods). This normalization procedure allowed us to pool the retinotopic
218 maps of all imaging planes into a single plane. We generated this pooled plane for both ON and
219 OFF subfields with both altitude and azimuth coordinates. The results showed a clear
220 retinotopy gradient for both ON and OFF subfields (Fig. 5e). Consistent with the established
221 retinotopic map of mouse V1 (Garrett et al., 2014; Zhuang et al, 2017): the altitude increases
222 along the anterior-posterior axis and azimuth increases along the lateral-medial axis. More
223 importantly, the retinotopic gradient appears smoother and less noisy for OFF subfields than
224 ON subfields in both altitude and azimuth. To quantify the retinotopy gradient, we performed
225 linear regression of the normalized altitude and azimuth against anterior/posterior and
226 lateral/medial locations, respectively. As expected, the data points with ON subfields spread
227 wider along the regression line than those with the OFF subfields for both altitude and azimuth
228 and more variance is explained by the regression for OFF units than ON units indicating greater
229 retinotopy scatter in ON subfields than in OFF subfields (Fig. 5f). When the same analysis was
230 performed for individual volumes, the differences in R^2 and standard error between ON and

231 OFF subfields were statistically significant (except the R^2 for altitude regression) and consistent
232 with the entire population (Fig. 6g,h, n=19, ON vs. OFF, standard error for altitude: 0.0078 ±
233 0.0011 vs. 0.0058 ± 0.0022 deg, T=37, p=0.02; standard error for azimuth: 0.0105 ± 0.0018 vs.
234 0.0085 ± 0.0043 deg, T=31, p=0.01; R^2 for altitude: 0.0318 ± 0.0075 vs. 0.0540 ± 0.0287, T=51,
235 p=0.077; R^2 for azimuth: 0.0713 ± 0.0119 vs. 0.1047 ± 0.0486, T=35, p=0.016. Wilcoxon rank
236 test).

237 In summary, the LGN inputs in the location channel are more numerous that ON inputs and
238 show less retinotopic scatter.

239

240 **Axon counts underlie spatial and functional specificity**

241 As described above, the motion (DS) and location (RF) input channels from LGN each have their
242 own functional specific spatial distribution in V1. For the motion channel, there are more nasal-
243 preferring boutons than temporal-preferring boutons in superficial layers and opposite in
244 deeper layers (Fig. 3a,b). One possibility of having such structure is that nasal-preferring axons
245 form more boutons in the superficial region and temporal-preferring axons form more boutons
246 in the deep region while keeping the axon numbers of both groups the same ("bouton model",
247 Fig. 6a left). Alternatively, one can have more nasal-preferring axons terminating in superficial
248 region and more temporal-preferring axons terminating in deep region while keeping the axon
249 arborization of both types similar ("axon model", Fig. 6a right). The "bouton model" predicts
250 different axon arborization between nasal- and temporal-preferring axons across depths and
251 different motion direction bias (NTIs) between the bouton population and the axon population,

252 while the “axon model” predicts similar axon arborization between nasal- and temporal-
253 preferring axons and similar motion direction bias between the bouton population and the
254 axon population. In favor of the “axon model”, our data show (1) axons have similar motion
255 direction bias as boutons (Fig. 4e-h); (2) no significant difference in NTI between boutons and
256 axons (Fig. 6b, bouton vs axon, superficial: n=49, 0.25 ± 0.06 vs. 0.27 ± 0.07, t=467, p=0.42;
257 deep: n=31, -0.23 ± 0.09 vs. -0.18 ± 0.09, t=153, p=0.25, Wilcoxon rank test); and (3) no
258 significant difference in axon morphology estimates between nasal-preferring axons and
259 temporal-preferring axons across depths (Supplementary Fig. 6a,b).

260 As with the motion channel, the difference in ON and OFF bouton counts in the RF units can
261 also be explained by either the “bouton model” or the “axon model” (Fig. 6c). Again, our data
262 supported the “axon model” by showing similar OFF dominance between bouton and axon data
263 (Fig. 5cd, Fig. 6d, ON-OFF index = $(num_{ON} - num_{OFF}) / (num_{ON} + num_{OFF})$, bouton vs. axon,
264 superficial: -0.235 ± 0.042 vs. -0.243 ± 0.042, n=72, t=1169, p=0.532; deep: -0.225 ± 0.05 vs. -
265 0.198 ± 0.05, n=48, t=376, p=0.072, Wilcoxon rank test) and no significant difference in axon
266 morphology between ON and OFF axons (Supplementary Fig. 6c,d). In summary, we found no
267 significant differences in axon morphology estimates within the DS and RF group, supporting
268 the model that axon distribution underlies the nasal/temporal bias in the DS group and the OFF
269 dominance in the RF group.

Discussion

Our study systematically investigated the functional properties and the spatial distributions of LGN-originated afferent axons in V1 with unprecedented labeling specificity. We found (1) the LGN inputs sensitive to motion (DS units) and LGN inputs sensitive to location (RF units) are largely separate with minimum overlap; (2) The units in the motion channels prefer lower TF and higher SF than units in the location channel; (3) the axons in the motion channel have more horizontal bouton spread than the axons in the location channel; (4) the motion channel shows depth-dependent motion direction bias; (5) the location channel shows OFF dominance independent of cortical depth; and (6) within each channel, the axon morphology is relatively uniform (Fig. 6). These findings support the notion that, in the thalamocortical projections of rodent visual system, there are functionally and structurally distinct parallel pathways similar to those in higher mammals.

Parallel pathways

Our findings are consistent with the general idea of the parallel pathway model in mouse visual system (Seabrook et al., 2017): the location information and motion information are passed to V1 by largely separate LGN afferent axons. Based on the model, our RF units most likely represent the classical X/Y-units (Cleland et al., 1971; Hoffmann et al., 1972), while our DS units may represent the W-units in cats (Wilson & Stone, 1975; Wilson et al., 1976). Furthermore, our results indicate that the DS axons have more extensive arbors in V1 than RF axons (Fig. 3d-g),

290 consistent with the morphological differences between W and X/Y LGN axons in cats (Gilbert &
291 Wiesel, 1979; Humphrey et al., 1985; Anderson et al., 2009). However, the DS units in our data
292 prefer low temporal and high spatial frequencies (Fig. 3ef) different from cat's W LGN cells
293 which prefer lower spatial frequency than X- and Y-cells (Sur & Sherman, 1982), but consistent
294 with the previous electrophysiology study in anesthetized mice showing DS LGN neurons prefer
295 high spatial and low temporal frequencies (Piscopo et al., 2013). On the other hand, our results
296 did not show pathway-specific laminar projection patterns as predicted by the model (DS axon
297 to superficial layers while RF axons to the middle layer, Cruz-Martin et al., 2014; Seabrook et al.,
298 2017). Instead, we found both RF and DS axons project uniformly throughout superficial to mid-
299 layers (Supplementary Fig. 2, 3), as had been reported before (Sun et al., 2016, but see Kondo
300 et al., 2016). In other species, LGN DS axons have been found to project mainly to layer 4 and 6
301 (Hei et al., 2014; Bereshpolova et al., 2019). Thus, how similar the DS cells in mouse LGN are to
302 the W-cells in cats and needs further investigation. Nonetheless, our results support the
303 notation that there are functionally specific parallel pathways in the feedforward projections
304 from LGN to V1 in the mouse.

305

306 **Preferred motion direction bias**

307 Consistent with previous studies (Marshel et al., 2012; Piscopo et al., 2013; Scholl et al., 2013;
308 Zhao et al., 2013; Cruz-Martin et al., 2014; Durand et al., 2016; Sun et al., 2016; Kondo et al.,
309 2016; Roth et al., 2016), we found significant portion of LGN units are direction-selective (22%
310 for axon, 23% for boutons, Fig. 3c, Supplementary Table 1). However, different studies reported

311 different distributions of preferred direction. Marshel et al. reported that the DS cells in
312 superficial LGN preferred nasal and temporal directions, while for LGN boutons in V1, Sun et al.
313 reported that almost all LGN DS axons preferred sharp nasal direction, and Kondo et al.
314 reported that the preferred directions of LGN DS axons slightly bias towards all four cardinal
315 axes. The differences among these studies are likely due to the different labeling strategies,
316 visual stimuli, and analysis parameters. In the current study, when pooling all DS units together,
317 the preferred directions strongly bias towards the nasal and temporal directions (Fig. 1n)
318 consistent with Marshel et al. This nasal/temporal direction biases have ethological relevance
319 since they can be used to detect self-generated motion during active behavior as has been
320 demonstrated at both retina (Sabbah et al, 2017) and visual thalamus (Roth et al., 2016).
321 Interestingly, our data show these two directions are represented at different cortical depth
322 with more nasal-preferring units in superficial layers and more temporal-preferring units in
323 mid-layers (Fig. 4).

324

325 **OFF dominance.**

326 It is well established in the early visual system of carnivores and primates that the visual
327 responses to dark stimuli (OFF) are faster and stronger than to bright stimuli (ON) (Jin et al,
328 2008, 2011; Yeh et al., 2009; Mazade et la., 2019; Kremkow et al., 2018). OFF responses are also
329 stronger in mouse V1 cells (Jimenez et al., 2018), similar to our findings in mouse LGN axons,
330 suggesting that such cortical organization may be inherited from LGN inputs. Our data further
331 show that the OFF subfields have less retinotopic scatter than ON subfields, another form of

332 OFF dominance underlying the orientation pinwheel structure in other species (Kremkow et al.,
333 2016; Lee et al., 2016). Considering that mouse V1 lacks a systematic orientation map (Ohki et
334 al., 2007), our results suggest such visual polarity dependent retinotopic organization may be
335 conserved across various visual cortical architectures through evolution.

336

337 **Technical considerations**

338 **Labeling bias.** It is possible that the Vipr2-IRES2-Cre-neo mice only labels a subset of all LGN
339 relay neurons. While this is difficult to disprove, we note that the proportions of the two main
340 functional types in our dataset (RS axon: 53%, DS axon: 22%) are similar to what has been
341 reported by previous electrophysiological study (RF cells: 52%, DS/OS cells: 11% Piscopo et al.,
342 2013; DS cells ~25%, Zhao et al. 2013), which argues against significant functional bias in our
343 labeling strategy.

344 **RF mapping.** We would like to point out that our criterion of defining significant RF is based on
345 responses to a sparse-noise stimulus similar to what has been used in previous studies (Zhuang
346 et al., 2013; Durand et la., 2016; de Vries et al., 2020). This method is effective if the unit
347 responds to brief small flashes but will perform poorly if the unit prefers more structured
348 stimuli, longer temporal durations or motion. As a result, our statement that DS LGN units tend
349 to not have significant spatial RF should be taken with caution: they may still prefer stimulus in
350 confined visual space locations, even if they do not possess sparse-noise mappable RFs.
351 Nonetheless, our conclusions about parallel pathways are unlikely to be undermined because
352 (1) a previous study with more structured mapping stimuli has shown similar functional

353 dichotomy (Piscopo et al, 2013); and (2) we found significant functional and structural
354 differences between RF axons and DS axons (Fig. 3e-j).

355 **Incomplete axon morphology.** The axon morphology estimates (bouton per axon, max bouton
356 distance, axon coverage area) of this study were performed on single 2-photon imaging planes
357 (~ 190 x 190 µm in xy and a few microns in z). Given that the arbor of an LGN axon in V1 can be
358 more than 500 µm in all three dimensions (Antonini et al., 1999), our measurements were
359 substantially incomplete. We reasoned that, with such crude measurements, any subtle
360 differences in axon morphology would fail to reach significance. However, to our surprise, the
361 DS axons and RF axons showed highly significant differences consistently across all three
362 measurements. This indicates there should be dramatic differences between DS and RF axons in
363 their full morphology. Further studies with more rigorous morphological reconstruction are
364 needed to test this prediction.

365 # Methods

366 **Surgery and animal preparation**

367 In total, six Vipr2-IRES2-Cre-neo mice (3 male, 3 female) were used in this study. The surgery
368 included a stereotaxic viral injection and a cranial window/head-plate implantation. During the
369 injection, a glass pipette back-loaded with a 1:3 mixture of AAV1-CAG-mRuby (custom made
370 from plasmid addgene 107744, titer: $1.6x10^{12}$ vg/ml) and AAV1-Syn (or CAG)-FLEX-GCaMP6s
371 (addgene: 100845-AAV1, titer $4.3x10^{13}$ vg/ml or 100842-AAV1, titer $1.8x10^{13}$ vg/ml,
372 respectively) was slowly lowered into left LGN (2.3 mm posterior 2.3 mm lateral from bregma,
373 2.6 mm below pia) through a burr hole. 5 minutes after reaching the targeted location, 200 nL
374 of virus mixture was injected into the brain over 10 minutes by a hydraulic nanoliter injection
375 system (Nanoject III, Drummond). The pipette then stayed for an additional 10 minutes before
376 it was slowly retracted out of the brain. Immediately after injection, a titanium head-plate and
377 a 5 mm glass cranial window were implanted over left V1 following the Allen Insitute standard
378 procedure protocol (de Vries et al., 2020; for detailed protocol see Goldey et al., 2014) allowing
379 *in vivo* two-photon imaging during head fixation.

380 After surgery, the animals were allowed to recover for at least 5 days before retinotopic
381 imaging with intrinsic signal during anesthesia (for detailed retinotopic protocol, see Juavinett
382 et al., 2017). After retinotopic mapping, animals were handled and habituated to the imaging
383 rig for two additional weeks (de Vries et al., 2020) before *in vivo* two-photon imaging.

384 All experiments and procedures were approved by the Allen Institute Animal Care and Use
385 Committee.

386

387 **Histology**

388 To characterize the Cre expression pattern, Vipr2-IRES2-Cre-neo mice were crossed with the
389 Ai14 reporter line (Madisen et al., 2010) to generate Vipr2-IRES2-Cre-neo/wt; Ai14/wt animals.
390 Mice heterozygous for both Cre and the reporter were perfused and brains collected. Briefly,
391 mice were anesthetized with 5% isoflurane and 10 ml of saline (0.9% NaCl) followed by 50 ml of
392 freshly prepared 4% paraformaldehyde (PFA) was pumped intracardially at a flow rate of 9
393 ml/min. Brains were immediately dissected and post-fixed in 4% PFA at room temperature for
394 3-6 hours and then overnight at 4 °C. After fixation, brains were incubated in 10% and then 30%
395 sucrose in PBS for 12-24 hours at 4 °C before being cut into 50 µm sections by a freezing-sliding
396 microtome (Leica SM 2101R). Sections with LGN and V1 were then mounted on gelatin-coated
397 slides and cover-slipped with Prolong Diamond Antifade Mounting Media (P36965,
398 ThermoFisher).

399 To verify the injection location and GCaMP expression, the brain tissues from all experimental
400 mice were collected and sectioned with a similar procedure after all imaging sessions with
401 additional steps with antibody staining to enhance the GCaMP signal before mounting and
402 coverslipping. During antibody staining, sections containing LGN and V1 were blocked with 5%
403 normal donkey serum and 0.2% Triton X-100 in PBS for one hour, incubated in an anti-GFP
404 primary antibody (1:5000 diluted in the blocking solution, Abcam, Ab13970) for 48-72 hours at

405 4 °C, washed the following day in 0.2% Triton X-100 in PBS and incubated in a Alexa-488
406 conjugated secondary antibody (1:500, 703-545-155, Jackson ImmunoResearch) and DAPI.

407 The sections were then imaged with Zeiss AxioImager M2 widefield microscope with a 10x/0.3
408 NA objective. Fluorescence from antibody enhanced GCaMP and mRuby3 were extracted from
409 filter sets Semrock GFP-1828A (excitation 482/18 nm, emission 520/28 nm, dichroic cutoff 495
410 nm) and Zeiss # 20 (excitation 546/12 nm, emission 608/32 nm, dichroic cutoff 560 nm),
411 respectively.

412

413 ***In vivo* two-photon imaging**

414 When recovery, retinotopic mapping, habituation was finished (usually more than three weeks
415 after initial surgery), thalamocortical axons from LGN labeled with GCaMP6s were evident in
416 superficial- and mid-layers (0 – 500 µm) in V1 through the cranial window (Fig. 1c, 1e). We
417 choose 8 depths for in vivo two-photon imaging (50, 100, 150, 200, 250, 300, 350 and 400 µm
418 below pia). Imaging was done in a columnar fashion: at each cortical location calcium activities
419 at 3-8 depths were imagedplane-by-plane over multiple sessions with a conventional 2-photon
420 microscope or in a single session with a multi-plane 2-photon microscope (described below) . In
421 both microscopes, a 16x/0.8 NA water immersion objective (Nikon 16XLWD-PF) was rotated to
422 24 degrees from horizontal to image visual cortex using a commercial rotating head (Sutter
423 MOM). mitted light was first split by a 735 nm dichroic mirror (FF735-DiO1, Semrock). The
424 short-wavelength light was filtered by a 750 nm short-pass filter (FESH0750, Thorlabs) and a
425 470-588 nm bandpass emission filter (FF01-514/44-25, Semrock) before collected as GCaMP

426 signal, while the long-wavelength light was filtered by a 538-722 nm band pass emission filter
427 (FF01-630/92-30, Semrock) before collected as mRuby signal. Image acquisition was controlled
428 using Vidrio ScanImage software for both scopes (Pologruto et al., 2003, Vidrio LLC). To
429 maintain constant immersion of the objective, we used gel immersion (Genteal Gel, Alcon).

430 Single-plane two-photon imaging. 4 mice were imaged with two-photon excitation generated
431 by laser illumination from a Ti:sapphire laser (Coherent Chameleon Ultra II) tuned to 920 nm.A
432 single z-plane (179.2 x 179.2 µm with 512 x 512 pixels resolution) was imaged for each session
433 at a frame rate of about 30 Hz with an 8 KHz resonate scanner (Cambridge Technology, CRS
434 8K).To maintain constant imaging depth automatic z-drift correction functions were
435 implemented for experiments using the MOM motors. Briefly, a correction z-stack (± 50 µm
436 from targeted depth, 2 µm step depth) was recorded before each imaging session and, during
437 the session, the current imaging plane was continuously compared to each plane in the
438 correction z-stack. If a drift in depth was detected, the stage was automatically adjusted to
439 compensate for the drift, thus maintaining constant imaging depth. We found this procedure
440 crucial to our experiments since the boutons are small objects and a few-micron-drift in depth
441 would result in imaging a different set of boutons.

442 Multi-plane two-photon imaging. The other two mice were imaged by a custom-built, multi-
443 plane two-photon microscope (DeepScope, Liu et al., 2018) in which a liquid crystal spatial light
444 modulator (SLM; HSP-512, Meadowlark Optics) shapes the pupil wavefront to implement fast-
445 focusing and adaptive optics. The objective pupil was slightly underfilled (~0.65 effective NA)
446 and correction of systemic aberrations was performed with fluorescent beads to maintain near

447 diffraction-limited focusing over a 200 um range. Two-photon excitation was produced by laser
448 light from a commercial solid-state laser (Spectra-Physic Insight X3 laser) tuned to 940 nm. With
449 this microscope, we simultaneously recorded calcium activity from planes at 5 different depths
450 (50, 100, 150, 200, 250 µm) in single imaging sessions. Individual frames (125 x 125 µm with
451 512 x 512 pixels resolution) were acquired at an overall framerate of ~37 Hz with a volume rate
452 of 7.4 HzThe DeepScope showed nearly zero z-drift for a prolonged duration (< 2 µm over 24
453 hours), so we did not implement z-correction in sessions using DeepScope.

454 In another set of experiments, we used DeepScope to assess the effect of adaptive optics
455 adjusted on individual animals. The correction procedure was similar to the method described
456 in Sun et al., 2016. For two mice, 1 µm beads (Thermo Fisher, F8821) were deposited on top of
457 the brain surface under the coverglass during the initial surgery. Prior to the imaging session,
458 modal optimization over 12 Zernike modes (up to j = 15 Noll ordering, excluding piston and tilt)
459 was run to identify the SLM pattern that maximized the beads' fluorescent signal. Then, during
460 the imaging session, this SLM pattern was put on and off alternatively for consecutive two-
461 photon imaging frames (one frame on, one frame off, …) and drifting gratings were displayed.
462 After imaging, the interleaving movie was separated into two movies: one with adaptive optics
463 and the other without. Bouton's tuning properties were then extracted from each movie and
464 compared against each other.

465 All imaging sessions were performed during head fixation with the standard Allen Institue Brain
466 Observatory *in vivo* imaging stage (de Vries et al., 2020).

467

468 **Visual stimulation**

469 All visual stimuli were generated by Retinotopic_Mapping python package
470 (https://github.com/zhuangjun1981/retinotopic_mapping, Zhuang et al., 2017) and displayed
471 by a 24-inch LCD monitor (ASUS PA248Q, frame rate 60 Hz, 1920 x 1200 pixels, mean
472 luminance 45.3 cd/m^2) placed 15 cm from the mouse's right eye (covering 120° x 95° of
473 monocular visual space). We displayed locally sparse noise and/or full-field drifting grating in
474 each imaging session to measure receptive fields and orientation/direction/spatial and
475 temporal frequency tuning properties, respectively. In most sessions, we also displayed a five-
476 minute full-field mid-luminance gray to measure spontaneous activity. For locally sparse noise,
477 bright and dark squares (5° x 5°) were displayed in a random sequence on a grid tiling the entire
478 monitor. At any given time, multiple squares could be displayed but the minimum distance
479 between those squares should be no less than 50°. Each square lasted 100 ms and in total was
480 displayed 50 times. For drifting gratings, the combinations of 12 directions (every 30°), 3 spatial
481 frequencies (SF, 0.01, 0.04 and 0.16 cpd) and 3 temporal frequencies (TF, 1, 4, 15 Hz) were
482 displayed. Each display lasted 1 second and was spaced by 1-second mean luminance grey
483 period. In total, 3 x 3 x 12 + 1 (blank) = 109 conditions were randomly displayed in each
484 iteration and the whole sequence contained 13 iterations. All stimuli were spherically corrected
485 so that they were presented with accurate visual angles on the flat screen (Zhuang et al., 2017)
486 and displayed by the Psychopy python software (https://www.psychopy.org/, Peirce et al.,
487 2019).

488

489 **2-photon Image preprocessing**

490 The recorded 2-photon movies for each imaging plane were first averaged every 5 frames
491 (Sutter scope) or every 2 frames (DeepScope), then were motion-corrected using rigid body
492 transform based on phase correlation by a custom-written python package
493 (https://github.com/zhuangjun1981/stia/tree/master/stia, Zhuang et al., 2017). To generate
494 regions of interest (ROIs) for boutons, the motion-corrected movies were further downsampled
495 by a factor of 3 and then processed with constrained non-negative matrix factorization (CNMF,
496 Pnevmatikakis et al., 2016) implemented in the CaImAn python library
497 (https://github.com/flatironinstitute/CaImAn, Giovannucci et al., 2018). The resulted ROIs were
498 normalized by subtracting the mean and dividing the standard deviation. Then pixels below 3
499 were set to 0. These ROIs were further filtered by their size (ROIs smaller than 1.225 µm2 or
500 larger than 12.25 µm2 were excluded), position (ROIs within the motion artifacts were
501 excluded) and overlap (for ROIs with more than 20% overlap, the smaller ones were excluded).
502 For each retained ROI, a neuropil ROI was created as the region between two contours by
503 dilating the ROI's outer border by 1 and 8 pixels excluding the pixels within the union of all
504 ROIs. The calcium trace for each ROI was calculated by the mean of pixel-wise product
505 between the ROI and each frame of the movie, and its neuropil trace was calculated in the
506 same way using its neuropil ROI. To remove the neuropil contamination, the neuropil
507 contribution of each ROI's calcium trace was estimated by a linear model and optimized by
508 gradient descendent regression with a smoothness regularization (Zhuang et al., 2017; de Vries
509 et al., 2020). Nonetheless, the estimates of neuropil contamination in our datasets were
510 generally low (percentage of neuropil signal that contributed to the ROIs signal: 11.5 ± 0.5%)

511 likely due to the small volume and sparse distribution of afferent axons in V1. For each imaging
512 session, a comprehensive file in Neurodata Without Borders (nwb) 1.0 format was generated to
513 store and share metadata, visual stimuli, all preprocessing results, and final calcium traces using
514 the "ainwb" package (https://github.com/AllenInstitute/nwb-api/tree/master/ainwb). As
515 reported previously, a high skewness is an indication of active calcium activity (Mukamel et al.,
516 2009, Dipoppa et al, 2018). The ROIs with skewness greater than 0.6 were defined as "active"
517 boutons and were included in the following study, while others were excluded (Supplementary
518 Table 1).

519 For the neuropil subtracted calcium traces with a minimum value below 1, an offset was added
520 to the whole trace so that the trace minimum was 1. Other traces were remain unaltered. This
521 procedure ensured a positive baseline for all units in the df/f calculation (below).

522

523 **Bouton clustering**

524 The correlation-based bouton clustering procedure was based on previously reported
525 algorithms (Liang et al., 2018) and exact same procedure was performed on each imaging
526 plane. First, we detected calcium events for each active bouton in the imaging plane. The
527 calcium trace was smoothed by a gaussian filter with sigma of 0.1 seconds. Then event onsets
528 were detected as up-crosses over a threshold of 3 standard deviations above the mean. A
529 period 3 seconds before and after each onset was defined as an event window and the union of
530 all event windows for a particular ROI was saved. Second, for any given pair of boutons, the
531 union of event windows from both boutons was calculated and the calcium trace within the

union window was extracted and concatenated for each bouton. Then a Pearson correlation coefficient of the two concatenated traces was calculated for this pair. By performing this procedure on every pair of active ROIs, we generated a correlation coefficient matrix for each imaging plane. We found the event detection important because it confined the correlation to the period only at least one bouton in the pair was active thus avoided correlating the noise during the inactive period. Third, the correlation coefficient matrices were further thresholded to reduce noise: the correlation coefficients for a given bouton were maintained if the coefficients were larger than 0.5 or if they exceeded 3 standard deviations above the mean value of all the coefficients between this bouton and all others. Otherwise, they will be set to 0. Third, a hierarchy clustering was performed to a given imaging plane using "1 – thresholded correlation coefficient matrix" as the distance matrix using Scipy.cluster.hierarchy library with a "weighted" method (https://docs.scipy.org/doc/scipy/reference/generated/scipy.cluster.hierarchy.linkage.html). For each imaging plane, we calculated a cophenetic correlation distance to evaluate the clustering performance. Fourth, we use a threshold of 1.3 to separate clusters since ~ 1.5 shows up as a relatively natural cut-off in the dendrograms. This threshold appeared somewhat conservative on the clustered correlation coefficient matrix (Fig. 2e). Fifth, after clustering, each cluster was identified as a separate axon and its calcium trace was calculated as mean calcium trace of all boutons belonging to this cluster, weighted by the sum of their ROI weights.

For each detected axon, three values were extracted to estimate the morphology: (1) bouton number of this axon (Fig. 3e, 4i, 5f); (2) maximum distance among all bouton pairs belonging to this axon (Fig. 3f, 4k, 5j); (3) area of the convex polygon encapsulated by all the boutons

554 belonging to this axon (Fig. 3g, 4l, 5h). For axons with only one bouton, the metrics 2 and 3
555 were set to be “nan” and were excluded from statistical analysis.

556 To generate stacked axon mask in Fig. 3d, we first selected axons with at least two boutons for
557 each group (DS axons or RF axons). Then the binary mask of each individual axon was rotated
558 and scaled into the same standard orientation (up: anterior, left: lateral) and centered to its
559 own center of mass. All centered axon masks were summed together to generate a summed
560 population axon mask for each group. Since the numbers of RF and DS axons were different, to
561 make fair comparison, each summed population axon mask was divided by its own maximum
562 value, generating a normalized population axon mask which is plotted in Fig. 3d. Axons with
563 both significant RF and direction selectivity were excluded from this analysis to avoid double
564 counting.

565

566 **Receptive field analysis**

567 We calculated the units’ classic receptive fields from their responses to the locally sparse noise
568 stimulus. For a given square stimulus at a particular location with a particular sign, the calcium
569 traces within the window around the square onsets were extracted and aligned by the square
570 onsets. An event-triggered average trace was then calculated as the mean trace across all
571 aligned traces. The mean value of the averaged trace in the window [-0.5, 0] seconds from the
572 onset was calculated as the baseline and event-triggered df/f trace was calculated as (average
573 trace - baseline) / baseline. The response amplitude to this particular square was then
574 calculated as the mean df/f in the window [0, 0.5] second from the stimulus onset. By repeating

575 this procedure for all squares presented in locally sparse noise stimuli, a 2d amplitude map was
576 generated tiling the entire visual space covered by the monitor for each sign ("ON" from bright
577 squares and "OFF" from dark squares). From the amplitude map, a z-score map was calculated
578 by subtracting the mean and dividing the standard deviation of the entire map. The z-score map
579 was then smoothed by a Gaussian filter with a sigma of 1 pixel and upsampled by a ratio of 10
580 with cubic interpolation. The resulting map was defined as the receptive field map with a
581 resolution of 0.5 degrees (Fig. 1g).

582 We defined a receptive field map with peak value exceeding 1.6 as having a significant classic
583 RF. The peak value of ON and OFF receptive field map combined was defined as RF strength
584 plotted in Fig. 3b. For the receptive field maps having a significant classic RF, the RF was
585 generated by thresholding either with a value of 1.6 (for maps with a peak less than 4) or with a
586 value of 40% of its peak (for maps with a peak greater than 4, Zhuang et al., 2013). The RF area
587 (plotted in Fig. 5b, 5d) was calculated as the area of the binary mask after thresholding. The RF
588 center (plotted in Fig. 5ij) was calculated as the location of the center of mass from the
589 weighted mask after thresholding.

590 For the retinotopy analysis in Fig. 5ij, we rotated and scaled each imaging plane so that they
591 had the same orientation of cortical surface (up: anterior, down: posterior, left: lateral, right:
592 medial) with same scale. For each of these planes, we obtained all significant RFs from boutons
593 in this plane and calculated their centers. The population RF was then calculated by summing all
594 significant RFs and thresholding with the same steps described above. Then the relative RF
595 location of each individual RF was calculated as the vector pointing from the population RF

596 center to the individual RF center. The relative RF locations were then normalized by
597 subtracting mean and dividing by standard deviation (z-score relative RF location). To generate
598 the normalized retinotopy map for each imaging plane, the individual z-score relative RF
599 locations were color-coded and plotted to the center of their boutons within the rotated and
600 scaled imaging plane. Since the retinotopy gradient is uniform across mouse V1 (Zhuang et al.,
601 2017), these procedures allowed us to superimpose the normalized retinotopy maps from all
602 imaging planes together. We performed this for ON and OFF subfields and altitude and azimuth
603 separately generating four retinotopic maps with respect to each sign and visual space
604 dimension (Fig. 5i). To quantify retinotopic gradient and scatter, we performed linear regression
605 between cortical locations and z-score relative RF locations from these four superimposed
606 retinotopic maps with relevant axis (anterior-posterior axis against altitude and medial-lateral
607 axis against azimuth, Fig. 5j).

608

609 **Grating response analysis**

610 The units' responses to drifting gratings were analyzed by the event-triggered average
611 procedure similar to the RF response analysis. The difference is the temporal window to
612 calculate response was [0, 1] second from the grating onsets since the duration of each grating
613 was 1 second. We first define a unit having significant responses to the drifting gratings if it
614 reached two criteria: 1) it responded to at least one grating condition with a z-score greater
615 than 3 and 2) the Oneway ANOVA analysis of df/f responses across all grating conditions
616 (including blank trials) had a p-value less than 0.01. For a unit that had a significant response to

gratings, its peak condition was defined as the conditions with the highest df/f response. Its direction tuning curve was extracted as its df/f responses to different directions with the TF and SF the same as the peak condition and, if the minimum response from this curve was below zero, an offset was added to the whole curve that the minimum was zero. Its SF and TF tuning curves were extracted by a similar procedure. From direction tuning curve, we calculated the global orientation index (gOSI) as

$$gOSI = \frac{\left|\sum R_j e^{i2\theta_j}\right|}{\sum R_j}$$

Where j represents different direction conditions, R represents df/f response in a given direction and θ represents the direction. The preferred orientation as the angle of $\sum R_j e^{i2\theta_j}$. We calculated global direction index (gDSI) as

$$gDSI = \frac{\left|\sum R_j e^{i\theta_j}\right|}{\sum R_j}$$

And the preferred direction as the angle of $\sum R_j e^{i\theta_j}$. From the SF tuning curve, we calculated the preferred SF as

$$peak\ SF = 2^{\left(\frac{\sum R_j log_2 SF_j}{\sum R_j}\right)}$$

Where j represents different SF conditions. From TF tuning curve, we calculated the preferred TF as

$$peak\ TF = 2^{\left(\frac{\sum R_j log_2 TF_j}{\sum R_j}\right)}$$

Where j represents different TF conditions. For the units that did not have significant grating response, all these measurements were set to be "nan". We defined a unit to be direction-selective if it had a gDSI greater than 0.5 and orientation-selective if it had a gOSI greater than 0.3.

For each imaging plane, we calculated a nasal-to-temporal index (NTI, see main text):

$$NTI = \frac{num_{nasal} - num_{temporal}}{num_{nasal} + num_{temporal}}$$

Where num_{nasal} is the count of DS units that had preferred direction in the range of [-45°, 45°] and $num_{temporal}$ is the count of DS units that had preferred direction in the range of [135°, 225°]. Only the planes with num_{nasal} + $num_{temporal}$ greater than 10 were included in the analysis. We also calculated an ON-OFF index:

$$ON - OFF\ Index = \frac{num_{ON} - num_{OFF}}{num_{ON} + num_{OFF}}$$

Where num_{ON} is the count of RF units that had only ON subfield and num_{OFF} is the count of RF units that had only OFF subfield. Only the planes with num_{ON} + num_{OFF} greater than 10 were included in the analysis.

The imaging preprocessing, nwb packaging, bouton clustering, receptive field analysis, grating response analysis, and functional type classification were performed by a custom-written python package "corticalmapping" (https://github.com/zhuangjun1981/corticalmapping/tree/master/corticalmapping).

653 **Statistics**

654 To control the variability across imaging planes (different axon/bouton density, vasculature
655 pattern, expression level), almost all statistics were extracted from each plane and separated
656 for different functional types if necessary. For statistics that only one number can be drawn
657 from each imaging plane (bouton/axon count, NTI, etc), they were presented as mean ±
658 standard deviation. For statistics that a population distribution can be drawn from each imaging
659 plane (gDSI, gOSI, peak SF/TF, RF strength, RF area, bouton per axon, max bouton distance,
660 axon qhull area), mean for each plane was calculated first and mean ± standard error was
661 reported across imaging planes. The comparisons between different functional types within
662 imaging plane were performed by Wilcoxon rank-sum test, and comparisons between imaging
663 planes were performed by Mann-Whitney U test since the distribution of the statistics were
664 highly skewed and non-gaussian. We have verified our results of these two tests by paired t-
665 test and independent t-test respectively, and they all agreed with the non-parametric tests (not
666 shown).

667

668

Acknowledgments

Funding was provided by the Allen Institute for Brain Science and award number NS104949 from the National Institute of Neurological Disorders and Stroke. Its contents are solely the responsibility of the authors and do not necessarily represent the official views of the National Institutes of Health and National Institute of Neurological Disorders and Stroke. We thank many staff members of the Allen Institute, especially the In Vivo Sciences team for surgeries and the Manufacturing and Processing Engineering team for hardware support. We wish to thank the Allen Institute for Brain Science founder, Paul G. Allen, for his vision, encouragement, and support.

679 # References

680 Anderson JC, da Costa NM, Martin KA (2009) The W cell pathway to cat primary visual cortex. J
681 Comp Neurol 516:20-35.

682 Antonini A, Fagiolini M, Stryker MP (1999) Anatomical correlates of functional plasticity in
683 mouse visual cortex. J Neurosci 19:4388-4406.

684 Bereshpolova Y, Stoelzel CR, Su C, Alonso JM, Swadlow HA (2019) Activation of a Visual Cortical
685 Column by a Directionally Selective Thalamocortical Neuron. Cell Rep 27:3733-3740 e3733.

686 Cleland BG, Dubin MW, Levick WR (1971) Sustained and transient neurones in the cat's retina
687 and lateral geniculate nucleus. J Physiol 217:473-496.

688 Cruz-Martin A, El-Danaf RN, Osakada F, Sriram B, Dhande OS, Nguyen PL, Callaway EM, Ghosh
689 A, Huberman AD (2014) A dedicated circuit links direction-selective retinal ganglion cells to the
690 primary visual cortex. Nature 507:358-361.

691 de Vries, S.E.J., Lecoq, J.A., Buice, M.A. et al. (2020) A large-scale standardized physiological
692 survey reveals functional organization of the mouse visual cortex. Nat Neurosci 23:138-151

693 Dhande OS, Stafford BK, Lim JA, Huberman AD (2015) Contributions of Retinal Ganglion Cells to
694 Subcortical Visual Processing and Behaviors. Annu Rev Vis Sci 1:291-328.

695 Durand S, Iyer R, Mizuseki K, de Vries S, Mihalas S, Reid RC (2016) A Comparison of Visual
696 Response Properties in the Lateral Geniculate Nucleus and Primary Visual Cortex of Awake and
697 Anesthetized Mice. J Neurosci 36:12144-12156.

698 Garrett ME, Nauhaus I, Marshel JH, Callaway EM (2014) Topography and areal organization of
699 mouse visual cortex. J Neurosci 34:12587-12600.

700 Gilbert CD, Wiesel TN (1979) Morphology and intracortical projections of functionally
701 characterised neurones in the cat visual cortex. Nature 280:120-125.

702 Grubb MS, Thompson ID (2003) Quantitative characterization of visual response properties in
703 the mouse dorsal lateral geniculate nucleus. J Neurophysiol 90:3594-3607.

704 Hei X, Stoelzel CR, Zhuang J, Bereshpolova Y, Huff JM, Alonso JM, Swadlow HA (2014)
705 Directional selective neurons in the awake LGN: response properties and modulation by brain
706 state. J Neurophysiol 112:362-373.

707 Hoffmann KP, Stone J, Sherman SM (1972) Relay of receptive-field properties in dorsal lateral
708 geniculate nucleus of the cat. J Neurophysiol 35:518-531.

709 Hubel DH, Wiesel TN (1962) Receptive fields, binocular interaction and functional architecture
710 in the cat's visual cortex. J Physiol 160:106-154.

711 Huberman AD, Wei W, Elstrott J, Stafford BK, Feller MB, Barres BA (2009) Genetic identification
712 of an On-Off direction-selective retinal ganglion cell subtype reveals a layer-specific subcortical
713 map of posterior motion. Neuron 62:327-334.

714 Humphrey AL, Sur M, Uhlrich DJ, Sherman SM (1985) Termination patterns of individual X- and
715 Y-cell axons in the visual cortex of the cat: projections to area 18, to the 17/18 border region,
716 and to both areas 17 and 18. J Comp Neurol 233:190-212.

717 Jimenez LO, Tring E, Trachtenberg JT, Ringach DL (2018) Local tuning biases in mouse primary
718 visual cortex. J Neurophysiol 120:274-280.

719 Jin JZ, Weng C, Yeh CI, Gordon JA, Ruthazer ES, Stryker MP, Swadlow HA, Alonso JM (2008) On
720 and off domains of geniculate afferents in cat primary visual cortex. Nat Neurosci 11:88-94.

721 Jin J, Wang Y, Lashgari R, Swadlow HA, Alonso JM (2011) Faster thalamocortical processing for
722 dark than light visual targets. J Neurosci 31:17471-17479.

723 Kondo S, Ohki K (2016) Laminar differences in the orientation selectivity of geniculate afferents
724 in mouse primary visual cortex. Nat Neurosci 19:316-319.

725 Kremkow J, Jin J, Wang Y, Alonso JM (2016) Principles underlying sensory map topography in
726 primary visual cortex. Nature 533:52-57.

727 Kremkow J, Alonso JM (2018) Thalamocortical Circuits and Functional Architecture. Annu Rev
728 Vis Sci 4:263-285.

729 Lee KS, Huang X, Fitzpatrick D (2016) Topology of ON and OFF inputs in visual cortex enables an
730 invariant columnar architecture. Nature 533:90-94.

731 Lennie P (1980) Parallel visual pathways: a review. Vision Res 20:561-594.

732 Liang L, Fratzl A, Goldey G, Ramesh RN, Sugden AU, Morgan JL, Chen C, Andermann ML (2018) A
733 Fine-Scale Functional Logic to Convergence from Retina to Thalamus. Cell 173:1343-1355.

734 Marshel JH, Kaye AP, Nauhaus I, Callaway EM (2012) Anterior-posterior direction opponency in
735 the superficial mouse lateral geniculate nucleus. Neuron 76:713-720.

736 Mazade R, Jin J, Pons C, Alonso JM (2019) Functional Specialization of ON and OFF Cortical
737 Pathways for Global-Slow and Local-Fast Vision. Cell Rep 27:2881-2894 e2885.

738 Nassi JJ, Callaway EM (2009) Parallel processing strategies of the primate visual system. Nat Rev
739 Neurosci 10:360-372.

740 Ohki K, Reid RC (2007) Specificity and randomness in the visual cortex. Curr Opin Neurobiol
741 17:401-407.

742 Piscopo DM, El-Danaf RN, Huberman AD, Niell CM (2013) Diverse visual features encoded in
743 mouse lateral geniculate nucleus. J Neurosci 33:4642-4656.

744 Reid RC, Alonso JM (1995) Specificity of monosynaptic connections from thalamus to visual
745 cortex. Nature 378:281-284.

746 Rompani SB, Mullner FE, Wanner A, Zhang C, Roth CN, Yonehara K, Roska B (2017) Different
747 Modes of Visual Integration in the Lateral Geniculate Nucleus Revealed by Single-Cell-Initiated
748 Transsynaptic Tracing. Neuron 93:767-776 e766.

749 Roth MM, Dahmen JC, Muir DR, Imhof F, Martini FJ, Hofer SB (2016) Thalamic nuclei convey
750 diverse contextual information to layer 1 of visual cortex. Nat Neurosci 19:299-307.

751 Sabbah S, Gemmer JA, Bhatia-Lin A, Manoff G, Castro G, Siegel JK, Jeffery N, Berson DM (2017)
752 A retinal code for motion along the gravitational and body axes. Nature 546:492-497.

753 Scholl B, Tan AY, Corey J, Priebe NJ (2013) Emergence of orientation selectivity in the
754 Mammalian visual pathway. J Neurosci 33:10616-10624.

755 Seabrook TA, Burbridge TJ, Crair MC, Huberman AD (2017) Architecture, Function, and
756 Assembly of the Mouse Visual System. Annu Rev Neurosci 40:499-538.

757 Siegle JH et al. (2019) A survey of spiking activity reveals a functional hierarchy of mouse
758 corticothalamic visual areas. bioRxiv:805010.

759 Stone J, Dreher B, Leventhal A (1979) Hierarchical and parallel mechanisms in the organization
760 of visual cortex. Brain Res 180:345-394.

761 Sun W, Tan Z, Mensh BD, Ji N (2016) Thalamus provides layer 4 of primary visual cortex with
762 orientation- and direction-tuned inputs. Nat Neurosci 19:308-315.

763 Sur M, Sherman SM (1982) Linear and nonlinear W-cells in C-laminae of the cat's lateral
764 geniculate nucleus. J Neurophysiol 47:869-884.

765 Wilson PD, Stone J (1975) Evidence of W-cell input to the cat's visual cortex via the C laminae of
766 the lateral geniculate nucleus. Brain Res 92:472-478.

767 Wilson PD, Rowe MH, Stone J (1976) Properties of relay cells in cat's lateral geniculate nucleus:
768 a comparison of W-cells with X- and Y-cells. J Neurophysiol 39:1193-1209.

769 Yeh CI, Xing D, Shapley RM (2009) "Black" responses dominate macaque primary visual cortex
770 v1. J Neurosci 29:11753-11760.

771 Zhao X, Chen H, Liu X, Cang J (2013) Orientation-selective responses in the mouse lateral
772 geniculate nucleus. J Neurosci 33:12751-12763.

773 Zhuang J, Stoelzel CR, Bereshpolova Y, Huff JM, Hei X, Alonso JM, Swadlow HA (2013) Layer 4 in
774 primary visual cortex of the awake rabbit: contrasting properties of simple cells and putative
775 feedforward inhibitory interneurons. J Neurosci 33:11372-11389.

776 Zhuang J, Ng L, Williams D, Valley M, Li Y, Garrett M, Waters J (2017) An extended retinotopic
777 map of mouse cortex. Elife 6:e18372.

778

Method References

Dipoppa M, Ranson A, Krumin M, Pachitariu M, Carandini M, Harris KD (2018) Vision and Locomotion Shape the Interactions between Neuron Types in Mouse Visual Cortex. Neuron 98:602-615 e608.

Giovannucci A, Friedrich J, Gunn P, Kalfon J, Brown BL, Koay SA, Taxidis J, Najafi F, Gauthier JL, Zhou P, Khakh BS, Tank DW, Chklovskii DB, Pnevmatikakis EA (2019) CaImAn an open source tool for scalable calcium imaging data analysis. Elife 8:e38173.

Goldey GJ, Roumis DK, Glickfeld LL, Kerlin AM, Reid RC, Bonin V, Schafer DP, Andermann ML (2014) Removable cranial windows for long-term imaging in awake mice. Nat Protoc 9:2515-2538.

Juavinett AL, Nauhaus I, Garrett ME, Zhuang J, Callaway EM (2017) Automated identification of mouse visual areas with intrinsic signal imaging. Nat Protoc 12:32-43.

Liu R, Ball N, Brockill J, Kuan L, Millman D, White C, Leon A, Williams D, Nishiwaki S, de Vries S, Larkin J, Sullivan D, Slaughterbeck C, Farrell C, Saggau P (2018) Multi-plane Imaging of Neural Activity From the Mammalian Brain Using a Fast-switching Liquid Crystal Spatial Light Modulator. bioRxiv:506618.

Madisen L, Zwingman TA, Sunkin SM, Oh SW, Zariwala HA, Gu H, Ng LL, Palmiter RD, Hawrylycz MJ, Jones AR, Lein ES, Zeng H (2010) A robust and high-throughput Cre reporting and characterization system for the whole mouse brain. Nat Neurosci 13:133-140.

Mukamel EA, Nimmerjahn A, Schnitzer MJ (2009) Automated analysis of cellular signals from large-scale calcium imaging data. Neuron 63:747-760.

Peirce J, Gray JR, Simpson S, MacAskill M, Hochenberger R, Sogo H, Kastman E, Lindelov JK (2019) PsychoPy2: Experiments in behavior made easy. Behav Res Methods 51:195-203.

Pnevmatikakis EA, Soudry D, Gao Y, Machado TA, Merel J, Pfau D, Reardon T, Mu Y, Lacefield C, Yang W, Ahrens M, Bruno R, Jessell TM, Peterka DS, Yuste R, Paninski L (2016) Simultaneous Denoising, Deconvolution, and Demixing of Calcium Imaging Data. Neuron 89:285-299.

Pologruto TA, Sabatini BL, Svoboda K (2003) ScanImage: flexible software for operating laser scanning microscopes. Biomed Eng Online 2:13.

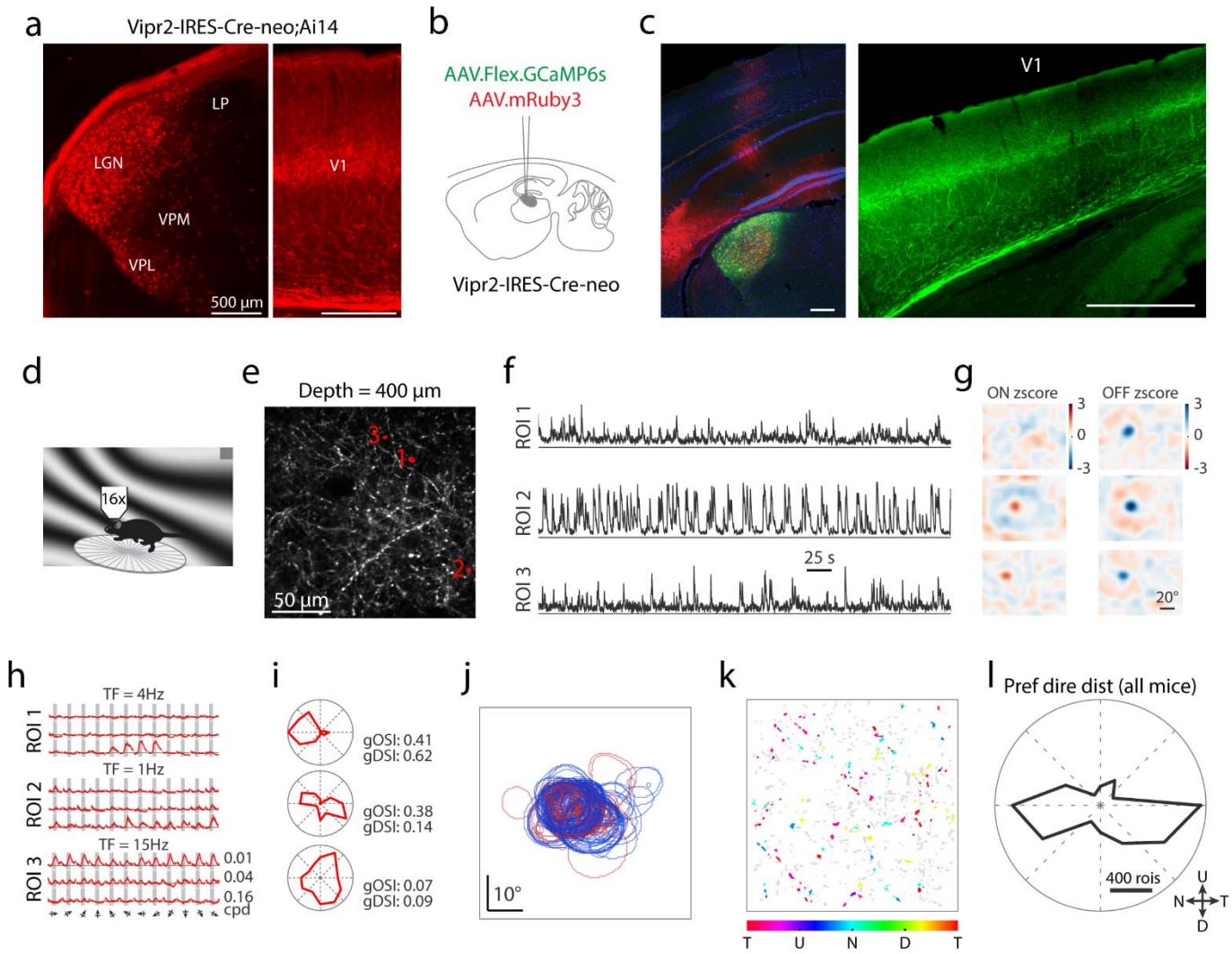

Figure 1. Vipr2-IRES-Cre-neo line specifically labels thalamocortical neurons in LGN. a, Histology showing tdTomato positive cells in LGN (left) and axons in V1 (right) from a Vipr2-IRES-Cre;Ai14 mouse. b, Strategy to label LGN originated thalamocortical axons. c, Histology showing GCaMP positive cells in LGN (left) and axons (right) in V1 from a mouse prepared as in b. Note the leaky mRuby expression along the injection track (left). Red: mRuby. Green: GCaMP6s (antibody enhanced) d, Sketch of in vivo imaging setup. e, Mean projection of calcium activities from an example imaging plane at 400 µm below pia. The calcium activities and response properties of the three marked ROIs are shown in panel f-i. f, Calcium traces after neuropil subtraction from the three example ROI marked in e. g, The ON and OFF zscore receptive fields. h, The averaged calcium responses of these three ROIs to different drifting grating conditions. All ROIs are measured by gratings with three temporal frequencies (1, 4 and 15 Hz), but only the responses to the peak temporal frequencies are shown here. i, The orientation/direction tuning curves. j, All significant receptive fields measured from the example imaging plane in e. Each contour represents one subfield. k, Spatial distribution of preferred direction of the example imaging plane in e. Grey color indicates no significant response to gratings or low direction selectivity. l, Distribution of preferred direction of all direction selective ROIs. N, nasal; T, temporal; U, up; D, down.

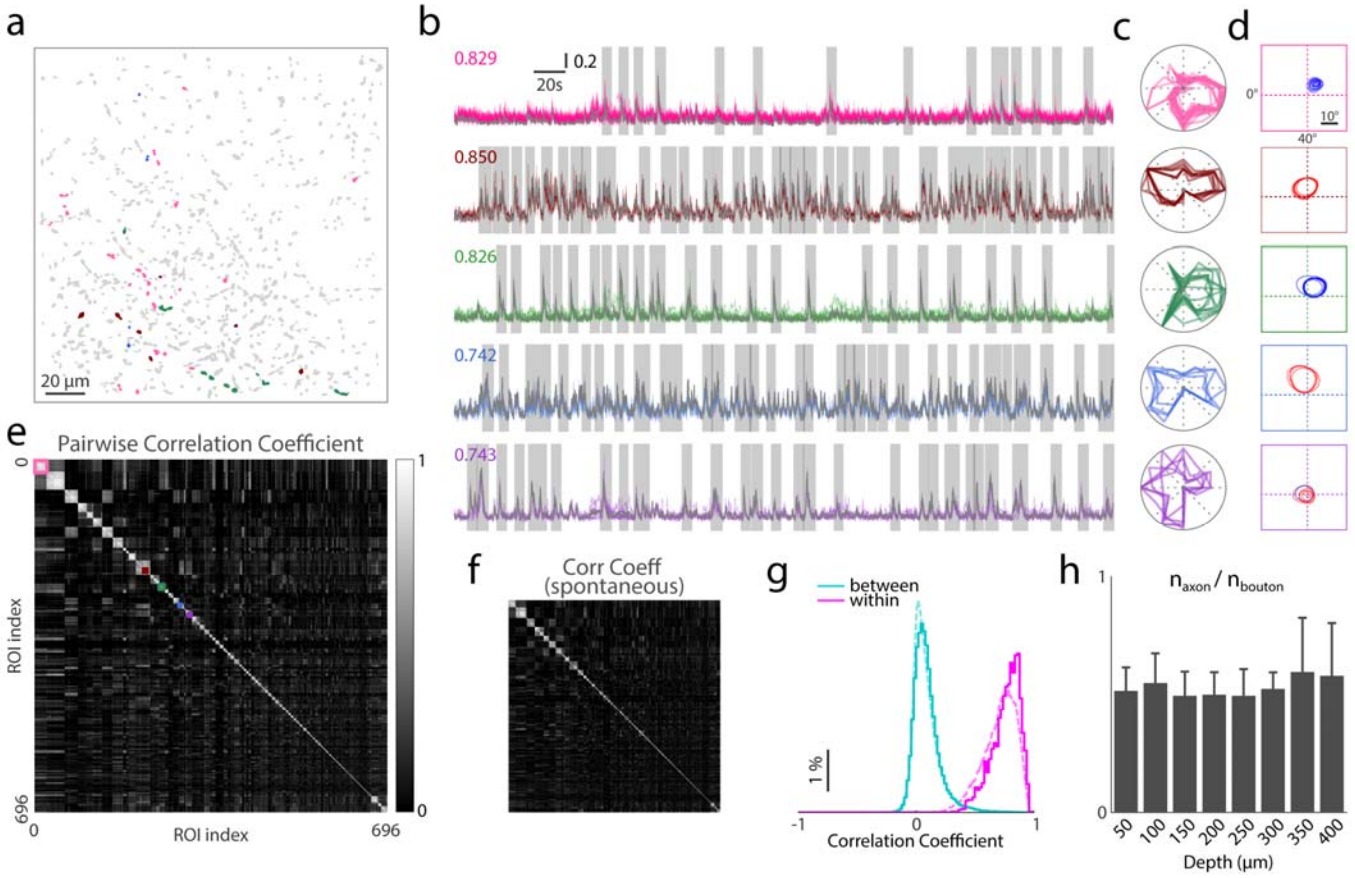

Figure 2. Boutons can be grouped into axons by pair-wise correlation based hierarchical clustering. a, An example imaging plane showing all active ROIs (grey) and 5 example axons (colored). The calcium activities, direction tuning curves and receptive fields of these 5 axons are shown in b-c, respectively. b, Calcium traces from the five marked axons. Traces from individual boutons (colored traces) and merged trace for the axon (gray traces) are superimposed. Vertical gray bars indicate detected events that were used for calculating pair-wise correlation coefficients (see Methods). Numbers are the mean pair-wise correlation coefficient for each axon. c, Superimposed orientation/direction tuning curves of individual boutons from each axon. d, Superimposed receptive fields of individual boutons from each axon. e, Clustered correlation coefficient matrix for the example imaging plane in a. Clusters for the five example axons in a are indicated by colored boxes. f, Same clustering applied to the correlation coefficients calculated from only spontaneous activity. g, Normalized distribution of correlation coefficients for between axon boutons and within axon boutons. Solid lines: data from the example imaging plane in a. Dashed lines: data from all imaging planes. h, Ratio between number of axons and number of boutons for each imaging plane across depth.

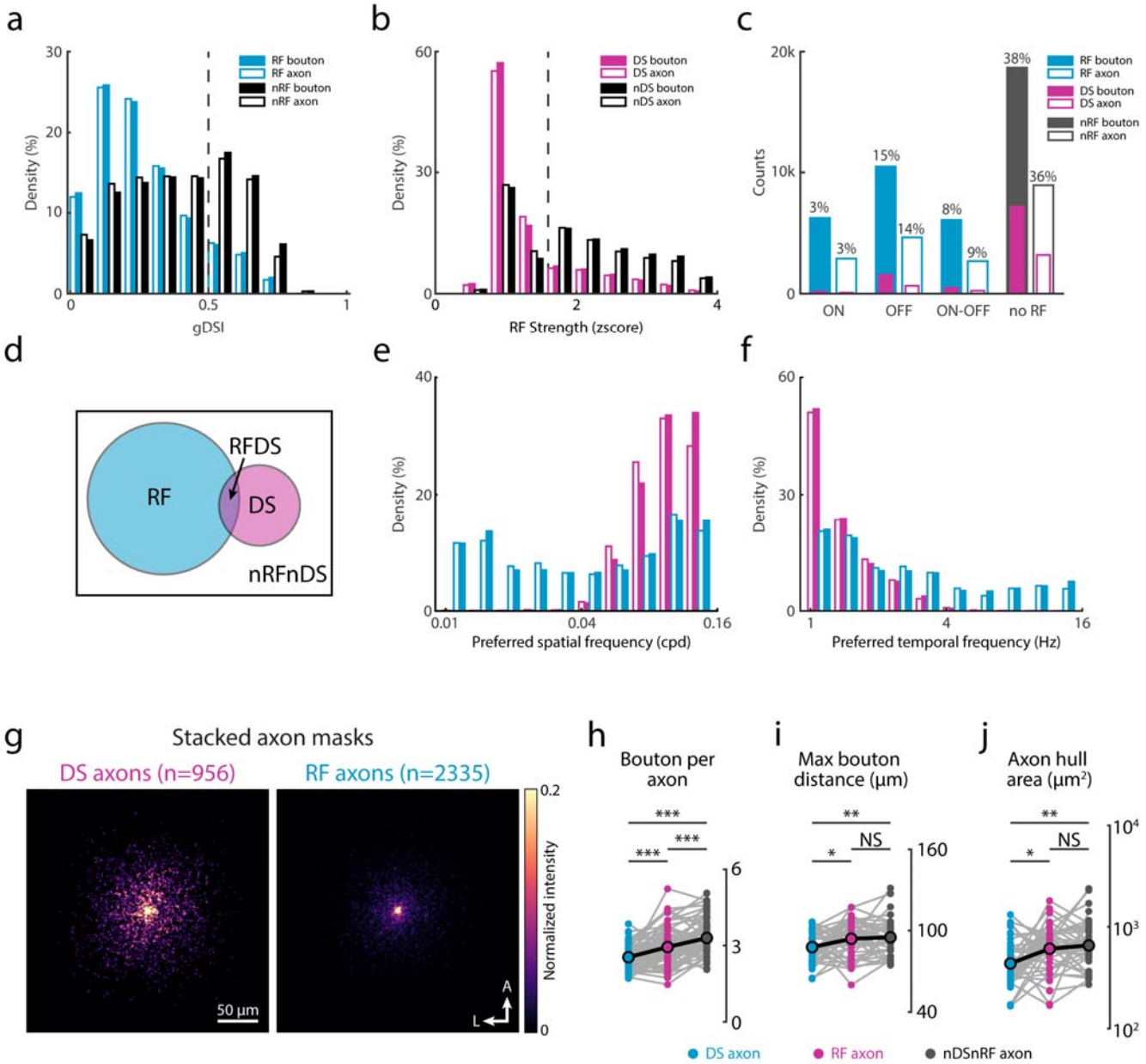

Figure 3. Feedforward inputs to V1 can be separated into two channels with distinct functional and structural properties. a, Distribution of gDSI of boutons/axons with or without significant receptive fields. RF: with receptive field. nRF: without receptive field. The dashed line represents the threshold for defining DS units. b, Distribution of receptive field strength of DS and non-DS units. DS: direction selective. nDS: non-direction selective. The dashed line represents threshold for significant spatial receptive field. c, Counts of each bouton/axon type. Units with receptive fields are broken into ON, OFF and ON-OFF groups. The percentage on top of each bar represents the portion of DS units in each group. e, Venn diagram describing relations between different populations. e and f, preferred spatial and temporal frequency distribution of DS units and RF units, respectively. g, Stacked axon masks for both DS axons and RF axons. Each axon mask was aligned to its individual center of mass before summed together. The summed masks were then divided by the maximum value to get normalized intensity (Methods). h-j, Comparisons of axon morphology estimates among different function classes (h: bouton number per axon; i: maximum bouton distance; j: area of convex hull encapsulated by all the boutons from a single axon). For analysis in e-j, axons that had both receptive fields and direction selectivity were excluded to avoid double-counting.

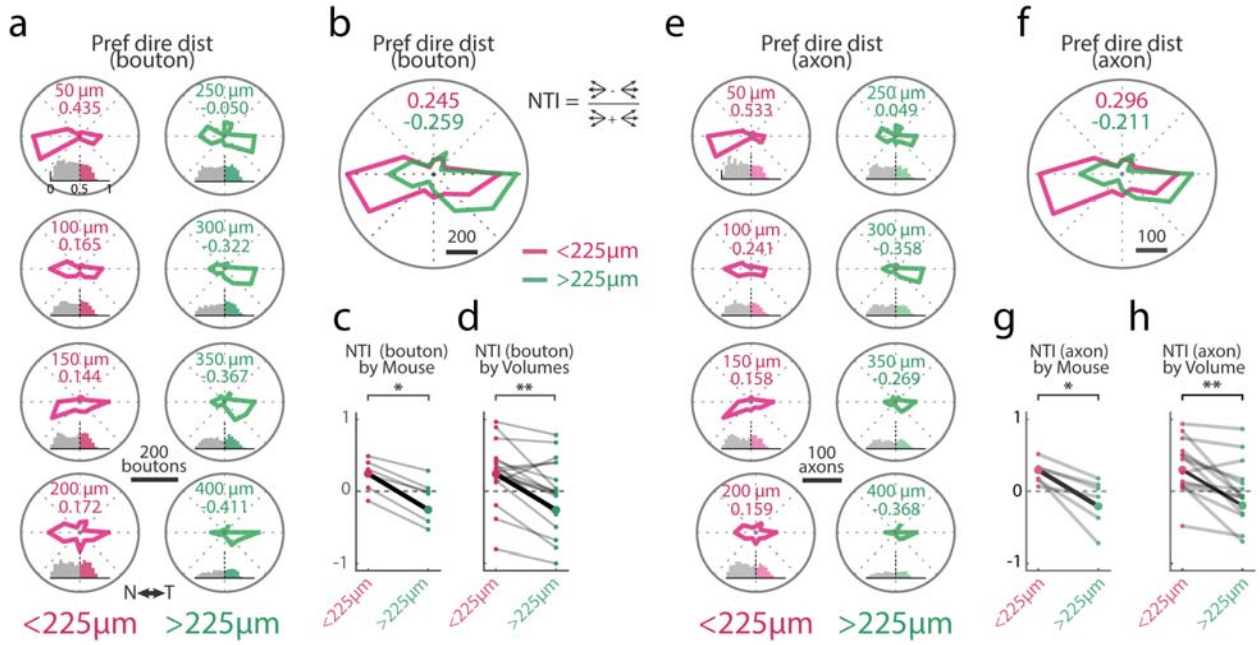

Figure 4. The DS LGN inputs show depth-dependent direction preference bias. a, Preferred direction distribution of DS boutons at each imaging depth. The number on top of each plot is nasal-to-temporal index (NTI). The histogram in each plot is the distribution of gDSI at the given depth. Vertical scale: 100 boutons. The vertical dashed line represents threshold for determining direction selectivity. b, Preferred direction distribution of superficial half vs. deep half of the entire dataset. c and d, Superficial vs. deep NTI comparisons for each mouse and each volume, respectively. e-h, same as a-d but for axons.

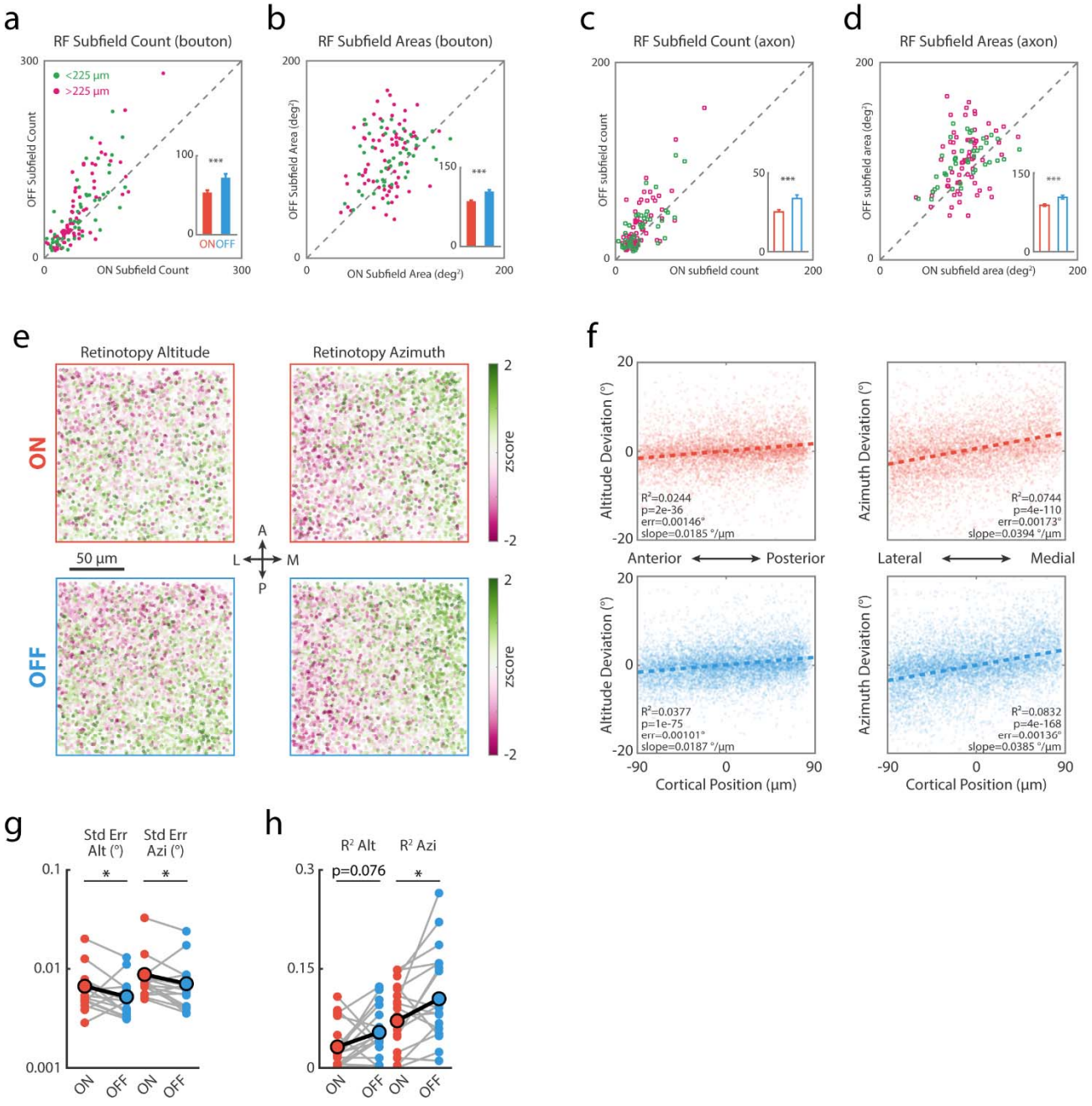

Figure 5. LGN inputs to V1 are OFF dominant. a and b, ON vs. OFF receptive subfield counts for each plane. c and d, ON vs. OFF receptive subfield area for each plane. e, Cortical retinotopy for boutons with significant receptive subfields. All imaging planes are pooled together after normalizing to same scale and orientation. Each dot is the center of mass of each bouton. Color represents normalized visual space coordinates centered at population average (Methods). Note the graduate change of altitude along anterior-posterior axis and azimuth along lateral-medial axis, and smoother retinotopy gradient of OFF subfields than ON subfields. f, The linear regression of retinotopy location against the cortical distance. Note the tighter spread along the regression line (larger R^2 and smaller standard error of estimate) of OFF subfields than ON subfields. g and h, ON vs. OFF regression standard error of estimate and R^2 for each imaged volume, respectively.

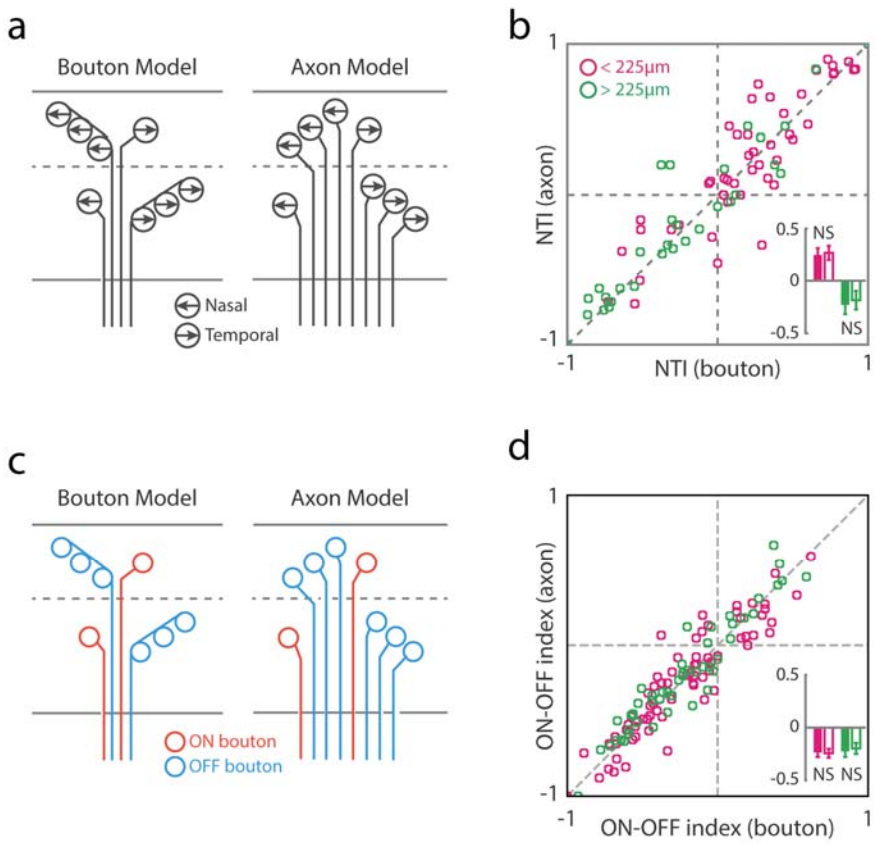

Figure 6. Functional specific bouton distribution can be explained by axon numbers of each group but not bouton per axon. a, two possible models (bouton model vs. axon model) that can give rise to the depth-dependent bias of motion direction preference. b, bouton vs. axon comparison of NTI for each imaged plane. c, Bouton model vs. axon model for OFF dominance. d, bouton vs. axon comparison of ON-OFF index for each imaged plane.

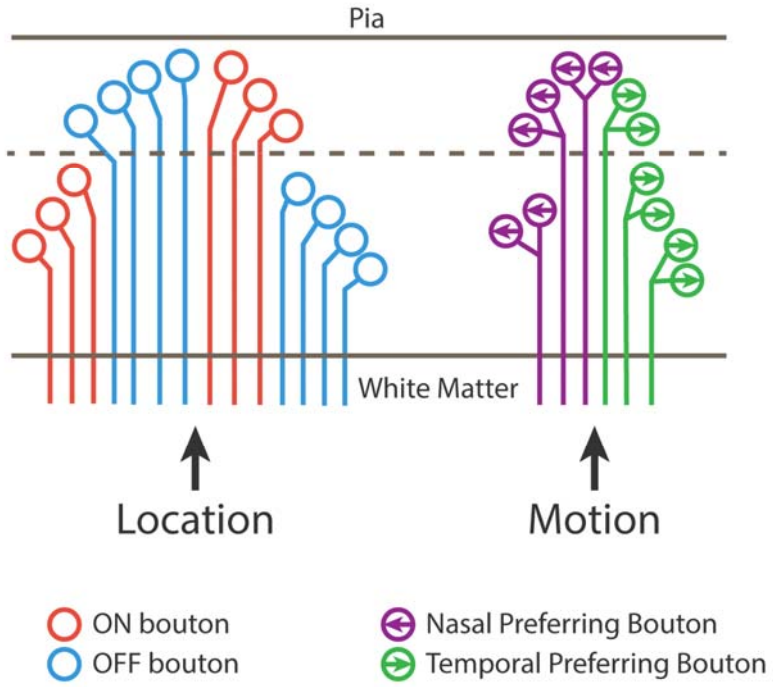

Figure 7. The spatial structure of feedforward information into mouse V1. (1) inputs can be split into two distinct channels, one with location information and the other with motion information; (2) the axons in location channel are more in number but smaller in arborization than axons in motion channel; (3) the motion channel shows depth-dependent motion direction bias; (4) the location channel shows depth-independent OFF dominance; and (5) axon morphology within each channel is uniform cross different functional subtypes.

Depth (µm)	Number of planes	Number of active units	Number of units with significant RF	Number of units responsive to gratings	Number of DS units
50	20	8120 (4002)	2374 (1009)	2396 (1237)	716 (353)
100	25	7347 (3862)	1368 (620)	1666 (887)	576 (283)
150	20	6924 (3330)	1505 (662)	1800 (921)	629 (309)
200	25	8469 (4128)	2050 (917)	2130 (1084)	761 (334)
250	20	7388 (3518)	1828 (804)	2030 (995)	758 (319)
300	20	6336 (3210)	1707 (832)	1536 (830)	609 (284)
350	9	3323 (1473)	904 (407)	1431 (637)	568 (221)
400	7	2264 (975)	569 (250)	982 (445)	442 (171)

Supplementary Table 1. Total unit counts at different imaging depths. Unit counts are presented as "bouton number (axon number)".

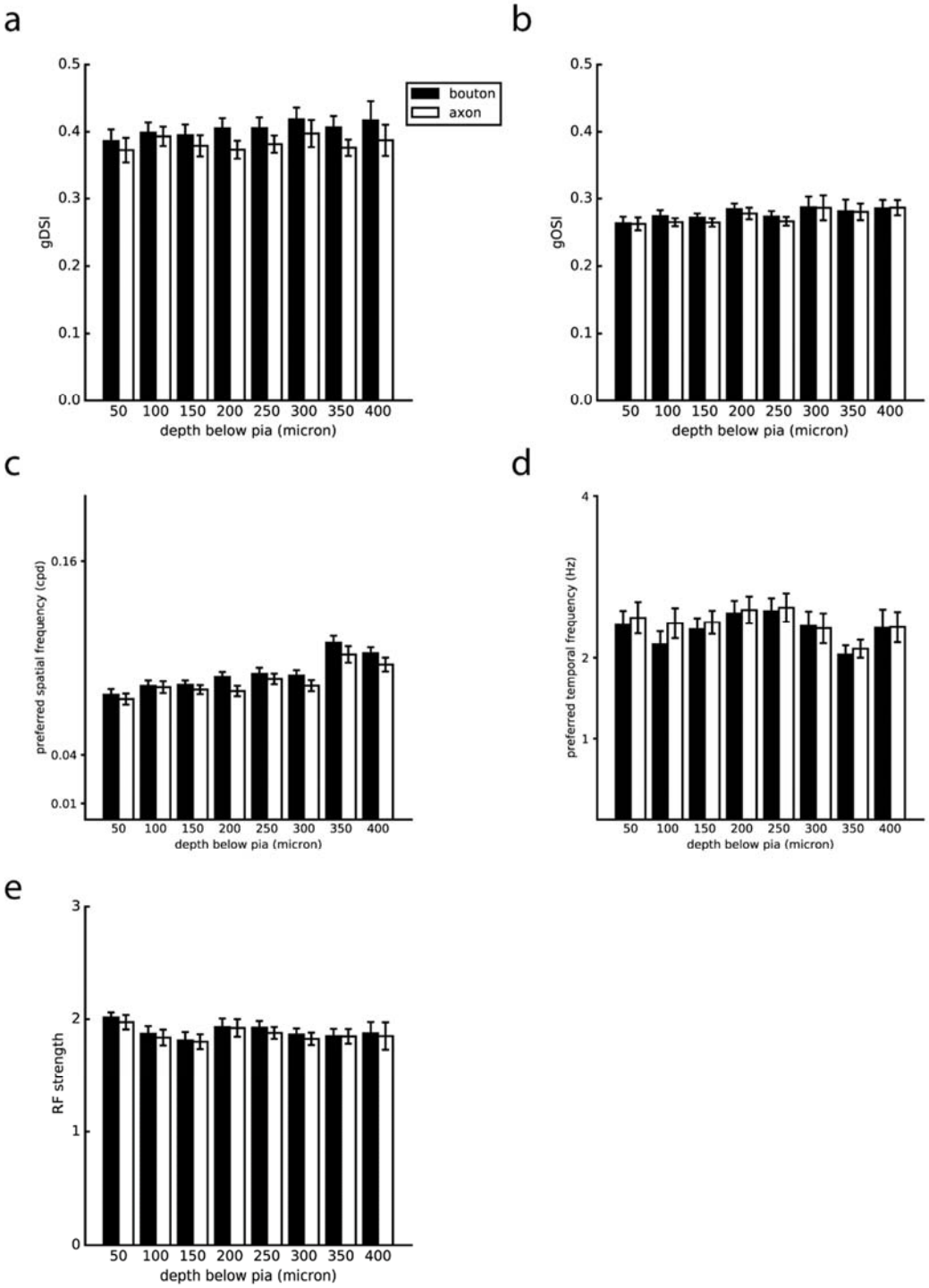

Supplementary Figure 1. Response properties at different depth. For panel a-d, only units with significant response to drifting gratings were included. For panel e, units with either significant receptive fields and/or significant response to drifting gratings were included. For each depth, averages of a given response propertie were calculated within each imaging plane at this depth and the mean and s.e.m. of these averaged values are plotted here.

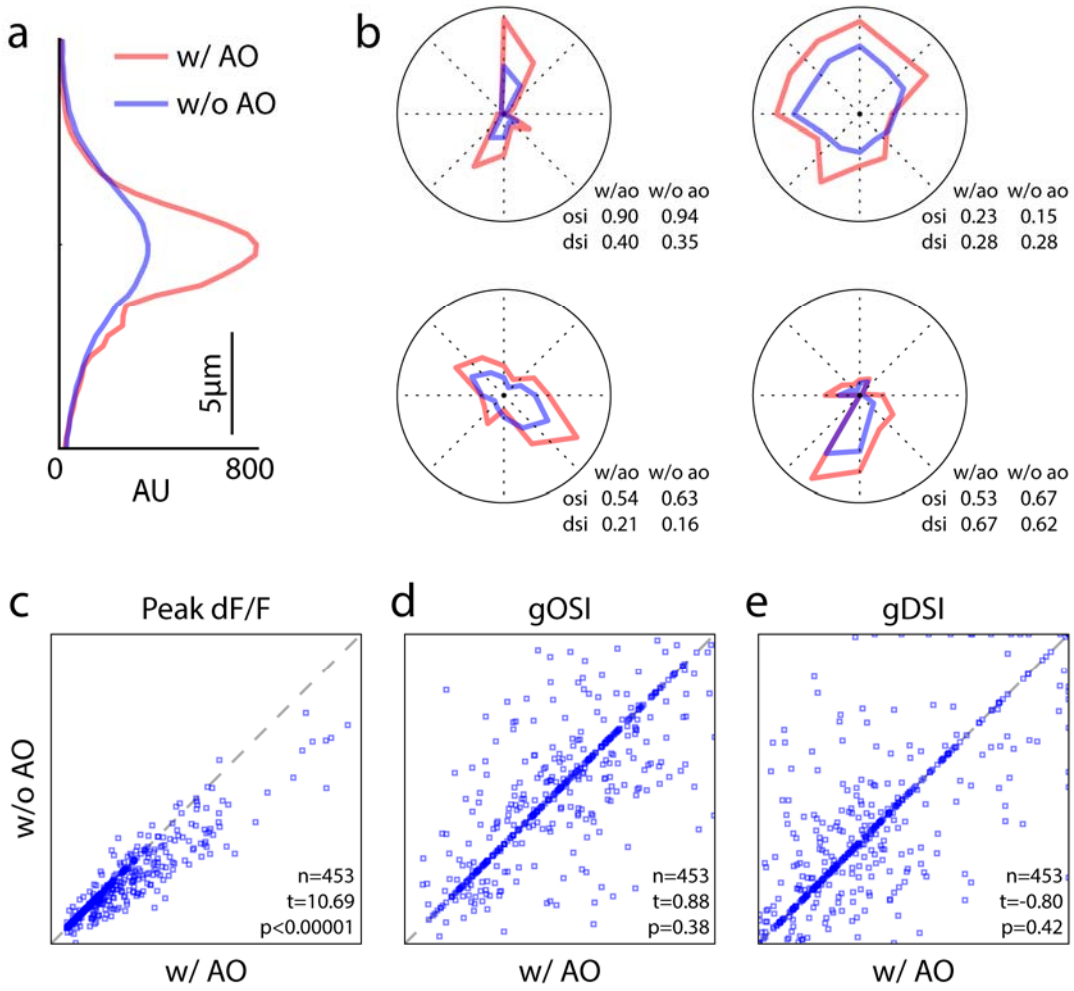

Supplementary Figure 2. Comparisons of response amplitude, direction selectivity and orientation selectivity between conditions with and without adaptive optics (AO). a, point spread function with and without (AO) by imaging 2 µm beads deposited between coverglass and surface of the brain in an awake mouse. b. example orientation/direction tuning curves from 4 example boutons. c-d, comparisons of peak dF/F, gOSI and gDSI of all recorded boutons. Two imaging planes in two mice (300 µm and 350 µm below pia). In AO conditions, laser beam wave front was corrected separately for each mouse.

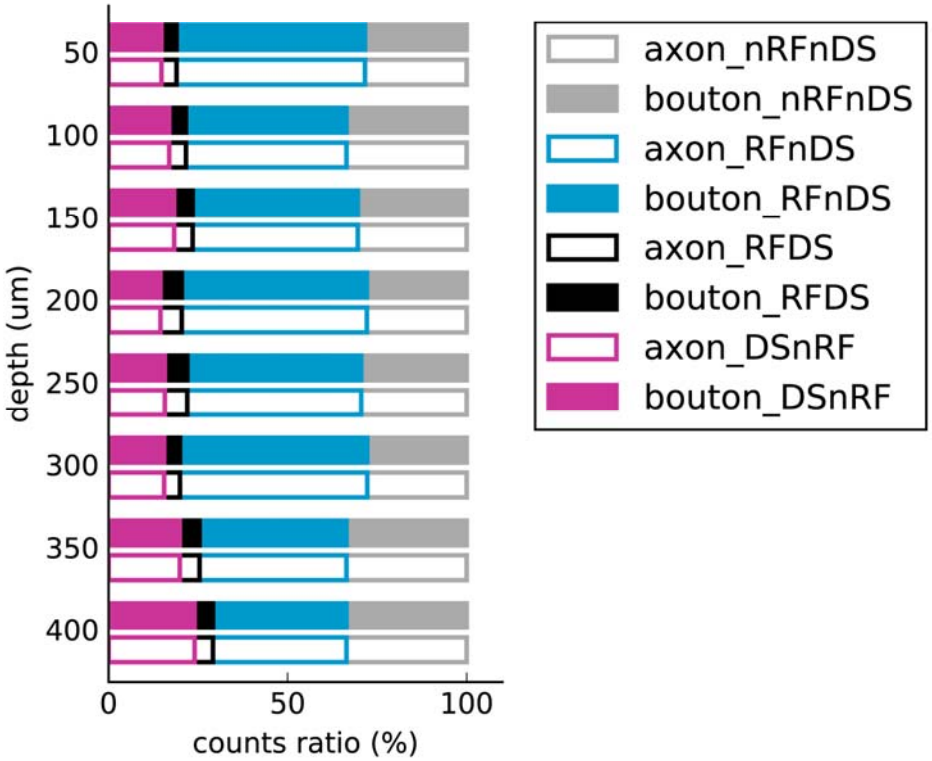

Supplementary Figure 3. The normalized distribution of the four non-overlapping functional types across depths. The proportion of each function type was calculated for each imaging plane and the means across all planes at given depth were plotted here. nRFnDS: units that did not have significant receptive fields and were not direction selective; RFnDS: units that had significant receptive fields but were not direction selective; RFDS: units that had significant receptive fields and were direction selective; DSnRF: units that did not have significant receptive fields but were direction selective.

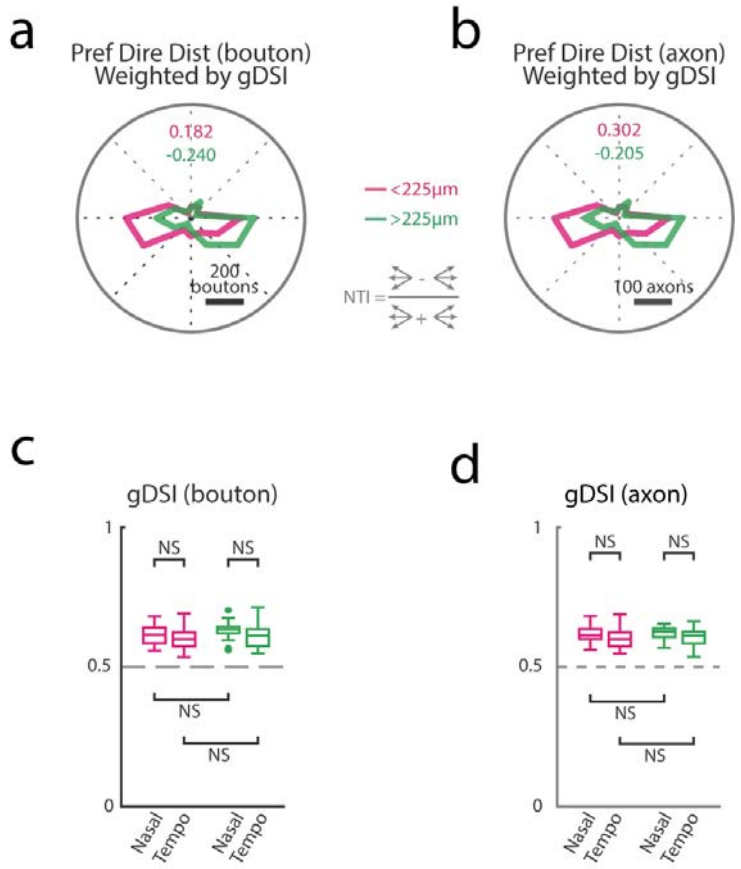

Supplementary Figure 4. Direction selectivity is similar between nasal- and temporal-preferring units across depth. a, same as Fig. 4b but for every bouton, its contribution to the distribution curve was weighted by its own gDSI so that the boutons with stronger direction selectivity would contribute more to the distribution. Thus, the count showed in this panel is smaller than Fig. 4b (gDSIs are no greater than 1), but the relative shapes of superficial and deep population remained relatively unchanged indication the depth-dependent bias trend was not a result of noise in gDSI measurement. c, gDSI comparisons between nasal- and temporal-preferring boutons at different depth. b and d, same as a and c but for axons, respectively.

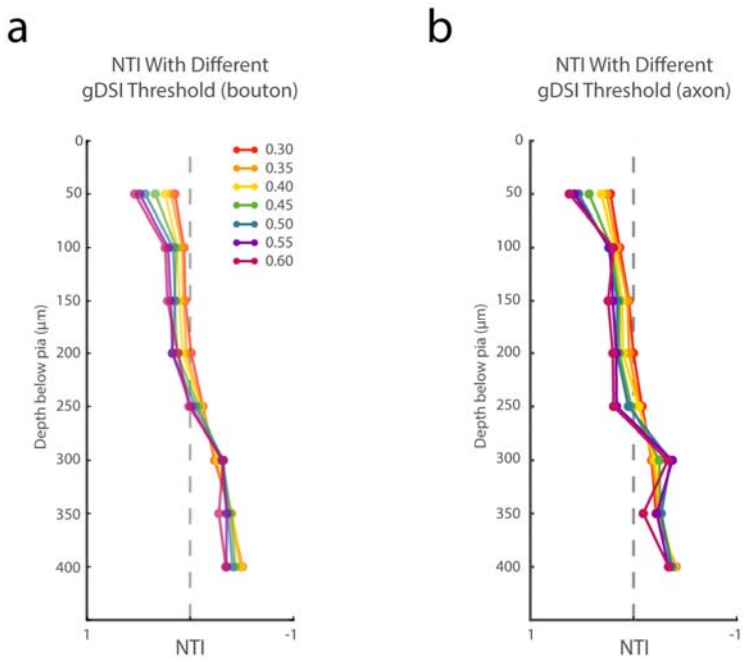

Supplementary Figure 5. Depth-dependent motion direction bias is robust across direction selectivity threshold for both boutons and axons. Different colored lines represent NTI along the depth measured with different direction selectivity thresholds. a, boutons. b, axons.

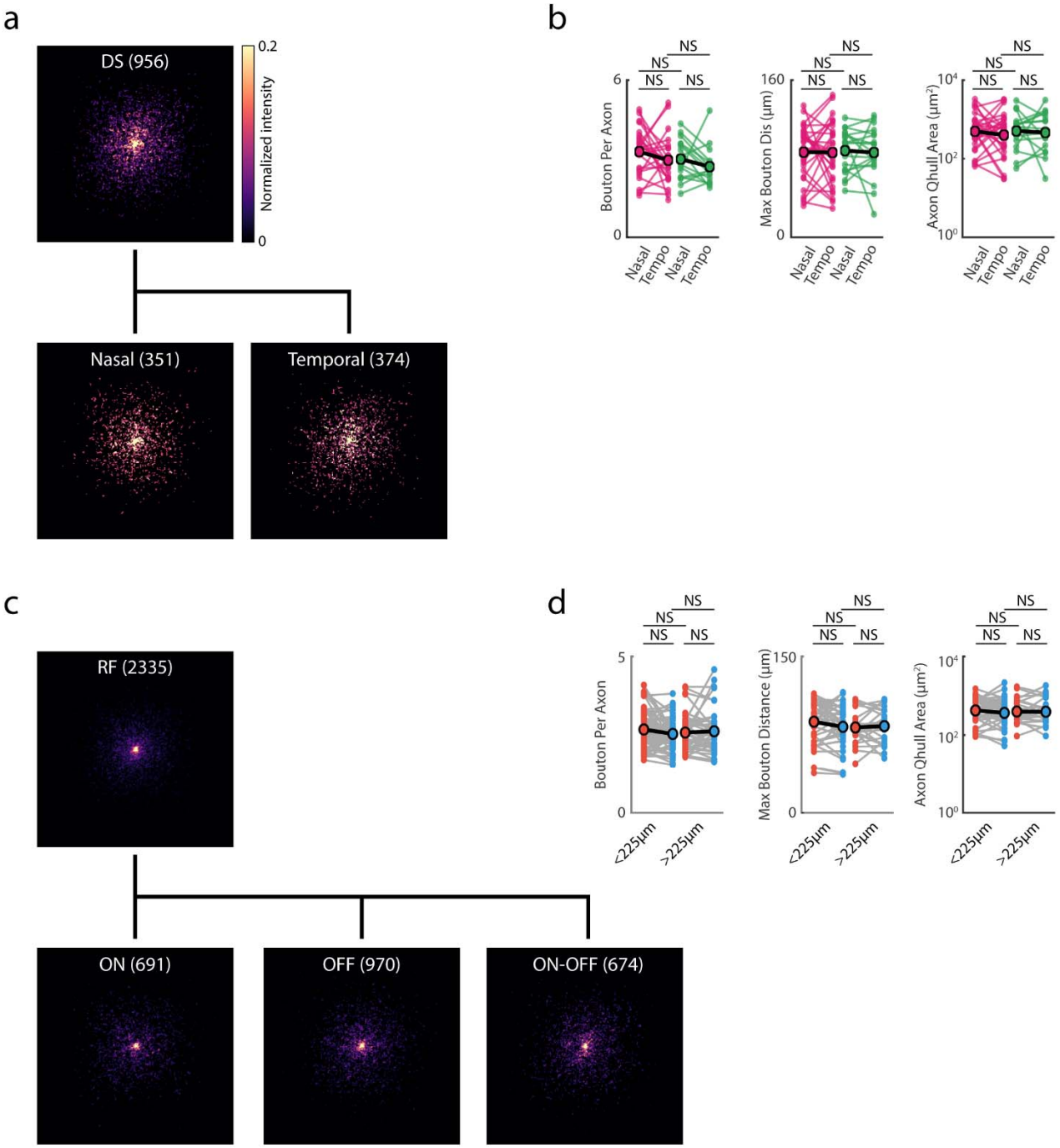

Supplementary Figure 6. Axon morphology estimates are uniform within DS and RF groups. a, stacked axon masks of nasal preferring and temporal preferring DS axons. b, comparisons of axon morphology estimates between these two groups. c, stacked axon masks of ON, OFF and ON-OFF RF axons. d, comparisons of axon morphology estimates between ON and OFF RF axons.

Supplementary Video 1. Two-photon images of calcium activities from LGN axons/boutons expressing GCaMP6s in V1 of an awake mouse. Imaging depth: 400 µm. Display speed 10x real time. Field of view: 179.2 x 179.2 µm. The image session is the same showed in Figure 1, e-l.